2019-04-01

Microfabrication and Characterization of Freestanding and Integrated Carbon Nanotube Thin Films

Derric Benjamin Syme
Brigham Young University

Microfabrication and Characterization of Freestanding and Integrated Carbon Nanotube Thin Films

Derric Benjamin Syme

A thesis submitted to the faculty of
Brigham Young University
in partial fulfillment of the requirements for the degree of

Master of Science

Brian D. Iverson, Chair
Brian D. Jensen
Richard Vanfleet

Department of Mechanical Engineering

Brigham Young University

ABSTRACT

Microfabrication and Characterization of Freestanding and
Integrated Carbon Nanotube Thin Films

Derric Benjamin Syme
Department of Mechanical Engineering, BYU
Master of Science

This work chronicles the fabrication of two unique thin films using carbon nanotubes. The first is a carbon film made primarily from vertically grown carbon nanotubes (CNTs) and rolled into lateral alignment. The second is an insulating film created by CNTs as a scaffolding to create a porous silica layer. Each topic represents a different method of utilizing CNTs for thin-film fabrication.

Investigation of an entirely carbon thin film, comprised of aligned and laterally oriented carbon nanotubes was performed. The thin film was strengthened by deposition of amorphous carbon for a total thickness of < 5 μm. This thickness is thinner than many previous films fabricated entirely out of carbon. Vertically aligned CNT arrays were manually rolled into a thin sheet and released from the growth substrate. Infiltration with amorphous carbon (as carbon coating) on the rolled CNTs was used to improve adhesion between neighboring CNTs after lateral alignment and to improve the mechanical integrity of the film. Mechanical property characterization indicated the ability to sustain a pressure differential across the film of up to 82.7 kPa for a suspended film of 4 mm in diameter. Peak stress, Young's modulus and biaxial modulus were obtained as a characterization of the strength of the thin film.

Fabrication and examination of a porous silica thin film, potentially for use as an insulating thermal barrier, was investigated. A vertically aligned CNT forest, created by chemical vapor deposition (CVD), was used as a scaffolding for the porous film. Silicon was deposited on the CNT forest using low pressure CVD (LPCVD), then oxidized to remove the CNTs and convert the silicon to silica – a material often used for electrical or thermal passivation. This fabrication method introduces hollow pores where the CNTs once occupied, further increasing the material's insulating properties. Thermal testing was performed by equating radiative and conductive heat transfer in a vacuum chamber and comparing the temperature difference between the film and a reference sample of comparable thermal resistance. For films approximately 50 μm thick, the thermal conductivity was found to be 0.054 - 0.071 $W/m \cdot K$.

Keywords: carbon nanotube, thin films, silica insulation, MEMs scaffolding

ACKNOWLEDGEMENTS

I would like to acknowledge Moxtek Inc. for their funding support in regards to the CNT thin films. I would like to thank Dr. Robert Davis, Dr. Richard Vanfleet, Dr. Brian Jensen, and Dr. Brian Iverson for their support, encouragement, and guidance. I will be eternally indebted to Dr. Iverson, specifically, who had many good reasons to give up on me but didn't, and who I learned much from in and out of academia.

Many of my peers were instrumental in this work. Jason Lund and Lawrence Barett helped me learn the basics of CNT growth. Joseph Rowley provided great expertise concerning bulge testing and Kevin Laughlin assisted with LPCVD silicon infiltration. Rydge Mulford contributed his wealth of knowledge towards thermal testing, and Kim Stevens assisted with tensile testing and provided insight into thermal testing apparatus design.

Lastly, I'd like to thank my wife, Kim, for her patience, love, and perseverance, and for caring for our beautiful daughter Audrey while I completed this work.

TABLE OF CONTENTS

LIST OF TABLES

LIST OF FIGURES

1 INTRODUCTION

Carbon nanotubes (CNTs) possess unique physical characteristics that make them ideal for a wide range of potential applications and have been of particular interest to the scientific community since the 1980s. Individual CNTs have excellent mechanical, electrical, thermal, optical, and chemical properties [1-3]. The versatility of CNTs and their exceptional properties allow them to be integrated into a variety of macroscale assemblies, including CNT mats, fibers, buckypapers, composites, and thin films [4-10].

One particularly important characteristic of the CNT is its strength. Individual CNTs have an elastic modulus of 1 TPa and a tensile strength of 100 GPa, making them among the stiffest and strongest of materials [1]. They are 10 times stronger than industrial fibers, and have a strength-to-weight ratio 600 times that of steel [6]. Concerning their electrical properties, they can carry a current density of nearly 4×10^9 A cm^{-2}, which is 1,000 times greater than metals like copper [8]. At 3500 W m^{-1} K^{-1}, CNTs have a thermal conductivity surpassing that of diamond [2, 5]. Finally, CNTs have an incredible length-to-diameter ratio, which make them useful for a variety of microelectromechanical (MEMS) devices. CNT growth heights of several hundred micron are easily achievable (lengths over 0.5 m have been obtained [11]), and with a diameter of just a few nanometers wide, practical length-to-diameter ratios can be greater than 10,000:1, providing relatively large surface area with little volume [4, 12]. The utility of these thermophysical and geometric properties makes CNTs intriguing as a thin film material.

The extensive versatility of the CNT offers great potential for integration into thin film applications. Broadly speaking, a thin film refers to a thin layer of material on a substrate that is very thick relative to the film. Thin-films are commonly vapor deposited or grown and are often associated with Si processing. Thin films are an important and rapidly growing area of MEMS research; carbon-based films have already proven beneficial in a number of applications. Favorable properties of CNTs in thin film fabrication include their large specific surface area, high porosity, high elasticity, low density, and, in some configurations, moderate transparency [12-17]. Applications of CNT films can be highly diverse. The tensile strength of CNTs makes them desirable for use in biosensing and biomedical fields, as the fibers can be sensitive to thermal, electrical, or chemical changes while also maintaining structural integrity [18-20]. The high electrical conductivity, due to ballistic transport of electrons within the CNT, makes them excellent for use in electrical systems. Due to their high porosity and specific area they have been used as both electrical current collectors for high-power supercapacitors and electrodes for energy storage and other devices [12, 21-23]. Highly flexible and transparent CNT thin films have been used as components in flexible solar cells or touch panels when deposited on plastics [13, 16]. Self-standing CNT films have been used as planar incandescent light sources that emit polarized radiation [17]. Additionally, the high thermal conductivity of CNTs allows for films to be used as efficient heat dissipaters for high-power devices [24-26].

Methods of CNT fabrication have been developed and optimized for a wide range of CNT uses. Research performed on CNTs at BYU is primarily done on vertically aligned CNTs (VACNTs), grown perpendicular to the base substrate using a process called thermal chemical vapor deposition (CVD). Before growth, a thin layer of aluminum oxide is deposited on a silicon wafer to prevent Fe catalyst from diffusing into the silicon substrate and to act as a resistor to

surface diffusion and sintering of the catalyst at high temperatures [27]. Using photolithography, patterned areas with photoresist can be created upon the substrate prior to depositing a metallic growth catalyst. A very thin layer of Fe is then thermally evaporated on the wafer and patterned using a photoresist, lift-off procedure. Patterned samples are heated in a furnace with a flowing gaseous carbon supply (ethylene) to initiate CNT formation. CNTs grow only in the regions of catalytic material, designated by lithography. The resulting CNT forest can be infiltrated by silicon, carbon, or some other material in subsequent CVD processing [28]. A film made primarily of CNTs will have many of the benefits listed in the preceding paragraphs. By infiltrating with other materials, it is possible to create a film with additional benefits, such as insulation.

Traditional insulating materials in MEMS, such as silicon oxide or silicon nitride, while having a much lower thermal conductivity than silicon, still have conductivities larger than required for many MEMs applications. Attempts to incorporate other insulating materials, such as silica aerogels, into micro devices have failed to preserve the material's low thermal conductivity [29]. Additionally, many insulating materials generally lack structural integrity and do not have a clear path for MEMs integration.

Recent work at BYU has shown that stable, microfabricated thin layer chromatography plates can be created using silica-coated CNTs [30]. Using CNT templated microfabrication (CNT-M), the CNTs can be infiltrated with silicon using low pressure CVD (LPCVD) and then oxidized at high temperatures to simultaneously burn out the carbon and oxidize the silicon, leaving only a porous silica structure, ideal for applications requiring insulation.

This work explores the methods and processes of fabricating two distinct CNT thin films using Carbon Nanotube Templated-Microfabrication. Both projects will capitalize on the high

length-to-diameter ratios present in CNTs to create high aspect-ratio structures. The first project is a purely-carbon, freestanding, thin film created from laterally aligned CNTs (see Chapter 2). This structure will use CVD to infiltrate a rolled CNT pattern with amorphous carbon to fill in voids and improve the films strength. Here, the CNTs act more as a structural layer within a composite material. The second project is an insulating silica film integrated into a silicon substrate using CNTs as a scaffolding to create a porous layer for minimizing heat transfer (Chapter 3). Here, CNTs are infiltrated with silica to improve structural strength and to act as a highly insulating thermal barrier. In addition to demonstrating the specific applications of the structures created here, this thesis will show the great potential CNTs have to be used as a framework for various microstructure designs.

2 ALIGNED AND LATERALLY ORIENTED CNT THIN FILMS

2.1 CNT Film Introduction

Various methods have been used to create CNT thin films. Early approaches include vacuum-filtering a well-dispersed CNT suspension onto a filtration membrane [31, 32]. Self-standing CNT films have been assembled layer-by-layer and patterned by standard lithography into electronics as demonstrated by low power, resistive, random-access memory [14]. Hyder *et al.* used layer-by-layer assembly, consisting of repeated, sequential immersion of a substrate into aqueous solutions of complementary materials, to create a highly conductive CNT/polymer composite film [22]. The inclusion of polymer in this application was used to create a positive electrode for lithium ion batteries. Other work has shown that vertically aligned CNT (VACNT) forests can be released directly from the growth substrate by floating-catalyst CVD (FCCVD) [24, 33]. CNTs are capable of deforming when released from the growth substrate; however, FCCVD was shown to provide high packing density and structural robustness to released CNT films.

The approaches to creating carbon thin films described above result in films that range from several hundred microns to several hundred nanometers thick. Wang *et al.* successfully reduced carbon film thickness using a microporous membrane to achieve laterally aligned CNT films (horizontal alignment within the plane of the thin film) from VACNT growth, and then compressed the membrane with a cylinder to flatten the forest into a 26 μm thick, paper-like

material [34]. The aligned CNTs adhered strongly to one another due to van der Waals forces, enabling the membrane to be released from the substrate on which they are grown using ethanol. Their work largely focused on the characterization of thermal and electrical properties for the resulting "buckypaper." Other buckypaper composites have been created using various methods, including shear-pressing [35, 36]. A comparison of the strength and modulus for comparable CNT and MEMs materials are shown in Table 2-1.

Table 2-1. Tensile strength and Young's Modulus for CNT and MEMs materials.

Material	*Tensile Strength (GPa)*	*Young's Modulus (GPa)*
CNT Film [35]	9.6	130
CNT Composite [36]	0.3	15
Carbon Nanotubes [3, 37, 38]	11 - 100	270 - 1000
Silicon [39-41]	1 - 7	50 - 190

This work demonstrates the creation of an entirely carbon thin film, comprised of aligned CNTs and strengthened by amorphous carbon, that are thin (< 5 μm) for use in x-ray applications where thickness can diminish signal strength. Similar work has been performed using polymer as a binder for the composite material [42]. The approach in this work is to create vertically grown CNT arrays that are rolled into a thin sheet to increase film strength in tension. We incorporate the use of a carbon coating on the rolled CNTs (or infiltration) to improve adherence between neighboring CNTs after lateral alignment and to improve the mechanical integrity of the film. We focus on mechanical property characterization in this study to indicate the ability to

sustain a pressure differential across the film. In the sections that follow, we describe the fabrication methods, report pressure differentials measured across the carbon thin film, and provide mechanical characterization of the thin films including tensile strength testing and surface roughness.

2.2 CNT Film Fabrication

2.2.1 Fabrication

Fabrication of the carbon thin film was designed to achieve multiple layers of overlapping CNTs. Unpatterned CNT forests were resistant to the flattening and aligning roller process. To create thin films with aligned fibers, CNT growth was patterned into rows (i.e. lanes, Figure 2-1) that would overlap when flattened. These lanes were then rolled in a direction perpendicular to the lane so as to achieve a thin film. Catalyst patterning and subsequent CNT growth followed established lift-off and high temperature growth processes [20, 43-46]. A 40 nm layer of alumina (Al_2O_3) was deposited on Si wafers using electron beam evaporation to provide a barrier to diffusion of Fe, and to act as a resistor to surface diffusion and sintering of the catalyst during the high temperature CNT growth [27]. Positive photoresist (AZ 3330, Integrated Micro Materials) was spun on the wafer at 2750 rpm for 60 s and then soft baked at 110°C for 60 s. The photoresist was patterned using lithography to selectively grow CNTs in rows on the wafer surface. Photoresist was exposed to a 350 W mercury bulb for 8 seconds and then baked at 110 °C for another 60 s before agitating in 300 Metal Ion Free developer (Integrated Micro Materials) for approximately 60 s. Patterned wafers were rinsed with deionized water and dried with N_2.

As a catalyst for CNT growth, 4 nm of Fe was deposited on the patterned photoresist using a thermal evaporator. Lift-off of the photoresist was performed by sonicating the wafer in N-Methyl-2-pyrrolidone (NMP) for 30 min (or longer, as needed) and then rinsed with acetone and isopropyl alcohol (IPA) to remove all photoresist. The lithographically defined Fe pattern consists of 10 μm wide lanes with 50 μm spacing (60 μm pitch). CNT growth height of these lanes is such that they span several gaps between neighboring lanes after rolling so as to create a film thickness comprised of several layers. These Fe lanes are connected by 5 μm wide horizontal rows, spaced every 250 μm and staggered from lane to lane (Figure 2-1). These thin, horizontal connections between rows of CNTs provide stability during CNT growth to achieve uniform vertical alignment across the wafer. To protect the patterned Fe catalyst, photoresist was spun on and soft baked at 110 °C before cutting to approximately a 2 cm^2 die using a Disco DAD-320 dicing saw. The photoresist was stripped with acetone and IPA, leaving only the exposed, patterned Fe.

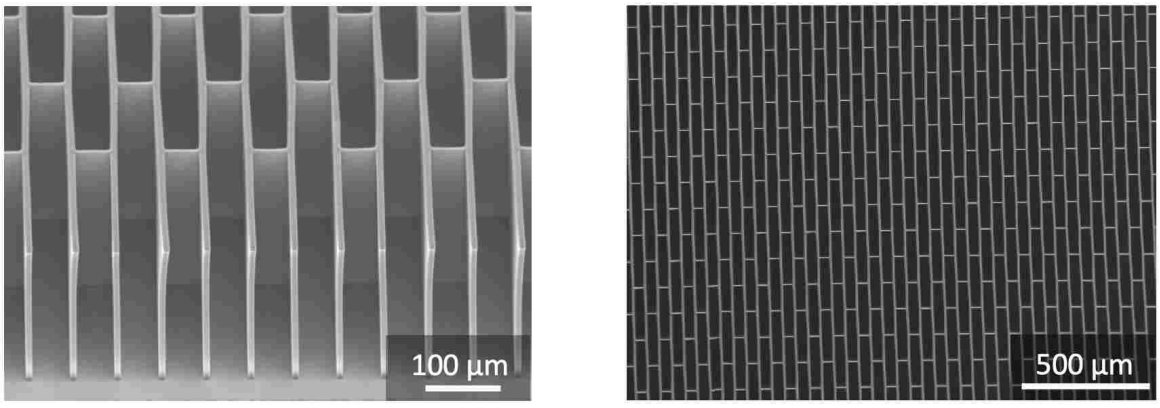

(a) (b)

Figure 2-1. (a) Lithographically patterned and vertically grown CNTs with connecting ribs to maintain vertical alignment. (b) Long-range order of the lanes of CNTs before rolling.

CNT growth was performed as follows. Diced samples were placed on a quartz boat in a Lindberg/Blue M Tube Furnace for CNT growth. While flowing hydrogen (H_2), the furnace was heated to 750 °C. Multi-walled CNTs were grown by flowing ethylene (C_2H_4) and H_2 for approximately 3 minutes at approximately 340 and 310 sccm, respectively, resulting in CNT growth heights of 180-200 µm. Growth heights were selected in order to span the gap to the base of the neighboring CNT lane and achieve significant overlap when the lanes are rolled. After 3 minutes, the C_2H_4 and H_2 were turned off and argon (Ar) was allowed to flow in order to purge the chamber for 1 min at the growth temperature. Subsequently, the furnace was turned off to allow the Ar to cool the sample. Vertically grown CNT patterns are shown in Figure 2-1.

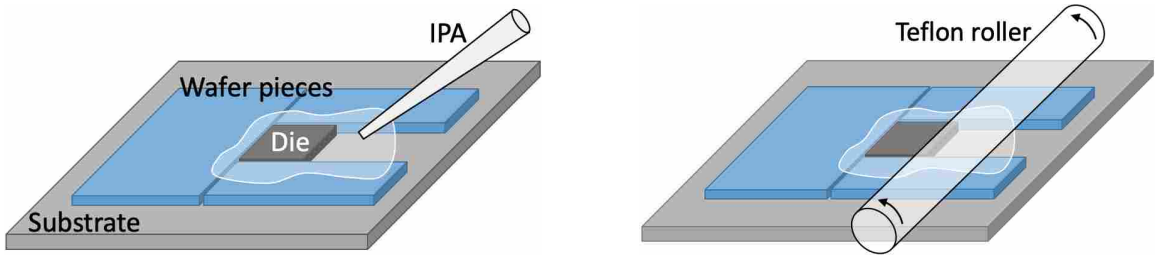

Figure 2-2. (a) Placement of the die with vertically grown CNTs among wafer pieces and lubrication with IPA. (b) Rolling of the CNTs to achieve lateral alignment with a Teflon roller.

In order to create a robust carbon thin film with aligned nanofibers, vertically grown CNTs were rolled to achieve a thin CNT sheet. Sample die were placed on a smooth surface with additional Si wafer pieces of the same thickness positioned on the sides of the sample to provide

an even rolling surface (Figure 2-2a). IPA was used to wet the CNTs and minimize CNT adhesion to the roller. Wetting was performed by flowing IPA in the direction of the desired lateral alignment and perpendicular to the 10 μm wide CNT lanes. A 0.5 in diameter Teflon cylinder was used to slowly roll the CNTs flat (Figure 2-2b). Rolled die were allowed to dry in ambient air. The schematic of Figure 2-3a illustrates the rolled, overlapping lanes of CNTs.

To decrease spacing between neighboring CNTs and improve adhesion between rolled lanes of CNTs, the rolled structure was coated/infiltrated with amorphous carbon. With the rolled, carbon thin film still attached to the substrate, it was placed in a furnace and heated to 900 °C in inert, flowing Ar until the process temperature was reached. At temperature, C_2H_4 and H_2 were again allowed to flow over the substrate at approximately 340 and 400 sccm, respectively, for 3 min and then purged and cooled with Ar, as before. The increased H_2 flow rate reduces the internal stresses of the film. Without this flowrate increase for H_2, the internal stress caused the film to curl dramatically before releasing from the substrate. Three minutes was sufficient time for the entire film to become infiltrated.

Following carbon infiltration, samples were released from the Si substrate by submerging in a potassium hydroxide (KOH) solution at room temperature, 30% by weight. The film generally released in <12 hours. Completed films were carefully removed from the KOH bath by placing the released film back on the Si substrate, placing the sample and substrate in a DI water bath, and then removing the sample from the DI bath with fine-mesh netting and tweezers to dry in ambient air.

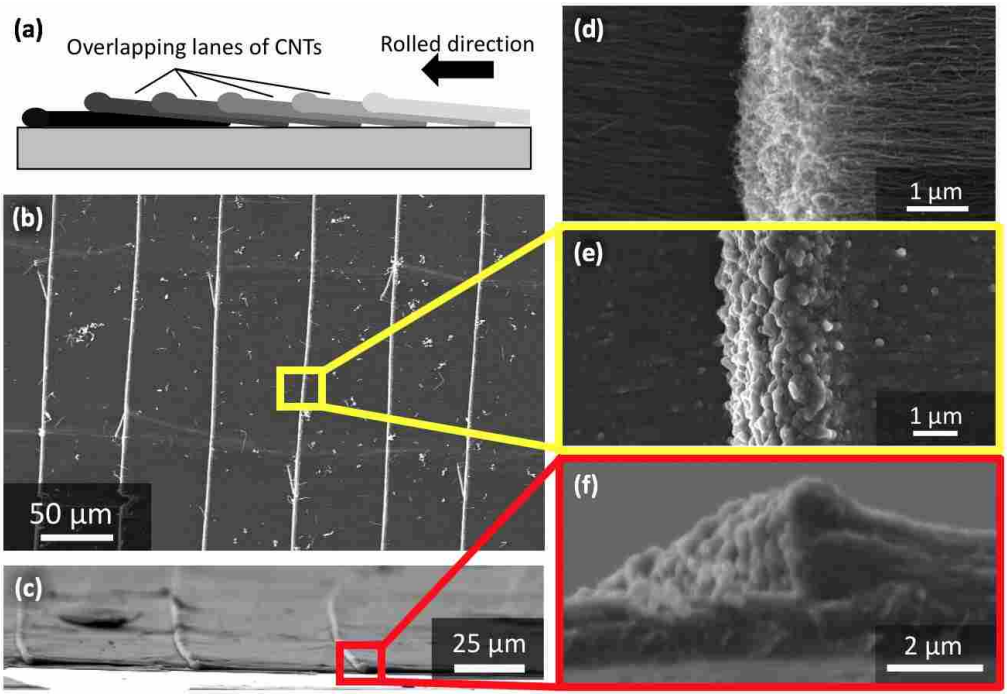

Figure 2-3. (a) Schematic of the laterally aligned CNT film after rolling. (b) Top-down and (c) side-view images of the film showing ridges formed from overlapping lanes. Top-down views of the ridges (d) before and (e) after infiltration with amorphous carbon. (f) Image of ridge and overall thickness of the carbon infiltrated film indicating regions of < 5 µm in thickness.

2.2.2 Sample Characteristics

Fabricated samples were inspected with scanning electron microscopy (SEM) to characterize dimensions and feature structure. Figure 2-3b and c are top-down and side-view images of a completed thin film and show the ridges formed from overlapping lanes. The ridge from one lane overlaps the CNTs from neighboring lanes, as the growth height is longer than the spacing between lanes. These ridges before and after infiltration with amorphous carbon are shown in detail in Figure 2-3d and e, respectively. The addition of the amorphous carbon provides additional binding between neighboring CNTs and reinforces the structure. A side-view

of the overlapping region after carbon infiltration is shown in Figure 2-3f. Here the thickness of the film is observed to be 4-5 μm towards the end of the overlapping regions and approximately 2 μm thick where there is no overlap. This 2 μm thickness is a significant reduction relative to multiple layers of lithographically defined 10 μm wide lanes.

Carbon infiltration provides significant benefits for film integrity and handling. Figure 2-4 illustrates a CNT thin film after rolling, with and without carbon infiltration. While both films remain delicate, the carbon infiltration increases film rigidity, decreases film waviness during the wet-handling stages and improves seating on the washer for drying and subsequent testing.

Figure 2-4. Carbon non-infiltrated and infiltrated samples placed on a washer after release from the Si substrate, with reduced film waviness indicating a more robust structure after carbon infiltration.

2.3 CNT Film Analysis Methods

2.3.1 Surface Roughness

The surface texture and roughness are important characteristics to consider because they can affect optical properties [47] and the ability of the film to be integrated into MEMS devices; a smooth surface is often a prerequisite base for many microstructures. A ZETA-20 3D optical profilometer was used to analyze surface characteristics and roughness. Among the measurements taken were the arithmetic mean (Sa), root mean square height (Sq), maximum peak and valley heights (Sp and Sv, respectively), distance between maximum peak and valley heights (Spv), skewness (Ssk), and kurtosis (Sku).

The arithmetic mean height (Sa) is the absolute value of the difference between the mean plane of the surface and the height of each point on the surface, given in equation (2-1),

$$Sa = \frac{1}{n}\iint_{n} |Z(x,y)|dx\,dy \tag{2-1}$$

where n is each point on the surface and Z is the height at that point. The root mean square height (Sq) is the standard deviation of heights, given by equation (2-2).

$$Sq = \sqrt{\frac{1}{n}\iint_{n} |Z^2(x,y)|dx\,dy} \tag{2-2}$$

Sp and Sv are the maximum peak and maximum valley heights, calculated as the absolute values of the maximum peak and valley heights relative to the mean height, respectively. Spv is the distance between the max peak and max valley (Sp + Sv).

Skewness (Ssk) is a measure of how symmetrical the peaks and valleys are around the mean plane; equation (2-3) for b = 3. An Ssk of 0 indicates symmetry, while a value greater than

0 indicates that the height distribution is skewed above the mean plane, and a value less than 0 indicates a height distribution skewed below the mean plane, as seen in Figure 2-5a. Finally, the kurtosis (Sku) is a measure of the sharpness of the profile; equation (2-3) for b = 4. An Sku of 3 indicates a normal height distribution, with rounded and sharp peaks equally likely. An Sku less than 3 indicates a height distribution skewed above the mean plane (rounded peaks) while an Sku above 3 means the peaks are sharp or spiky, as seen in Figure 2-5b.

$$\left.\begin{matrix} Ssk(b=3) \\ Sku(b=4) \end{matrix}\right\} = \frac{1}{Sq^b}\left[\frac{1}{n}\iint_n |Z^b(x,y)|dx\,dy\right] \tag{2-3}$$

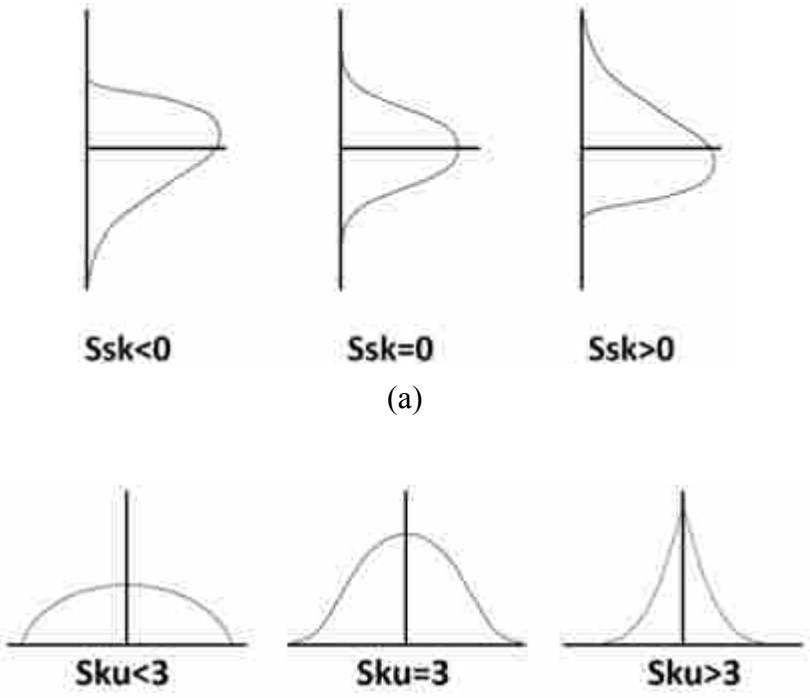

Figure 2-5. Skewness and kurtosis of a film's roughness. (a) The skewness (Ssk) represents the bias of the height distribution and the degree of symmetry about the mean plane. Values larger than zero indicate a distribution skewed above the mean plane and the predominance of peaks, while skewness below the mean plane (a prevalence of valleys) is indicated by values below zero. (b) The kurtosis (Sku) measures the roughness profile's sharpness. Values above 3 indicate a spiked height distribution, while values below 3 indicate broader height distributions.

2.3.2 Tensile Testing

To characterize the mechanical properties of the CNT films, tensile testing was performed. Tensile testing is a common and straight-forward method used to extract material properties and mechanical behavior of materials, as it can directly extract a film's behavior under load [48]. From tensile testing, the ultimate tensile strength and Young's modulus can be obtained. This data, combined with the results provided from pressure testing (applying a differential pressure across the film), can then be used to estimate Poisson's ratio of the material.

Researchers have used tensile testing to characterize free-standing thin films. Ruud *et al.* used tensile testing to find Young's modulus, Poisson's ratio, and the yield stress of Cu, Ag, and Ni films approximately 2 μm thick, with gauge sections of 10 mm by 3.3 mm [49]. Tensile testing samples in this work were prepared on Si die cut to the same gauge dimensions as Ruud *et al.* To investigate the potential isotropy of the material, two sample orientations were developed; one orientation in which the CNT patterns were grown parallel to the gauge length, and another grown perpendicular (see Figure 2-6). Dog-bone-shaped specimens are commonly used to provide a better gripping area, reduced slippage, and to prevent high stresses at the gripping locations that might affect test results. However, due to the constraints associated with sample size and thickness, as well as limits in the fabrication method used to prepare the thin films, a simple rectangular sample shape was selected [49].

Tensile testing (Instron 3342) was performed with a 1 lb JR S-Beam load cell. The upper end of each film was first attached to masking tape for handling purposes and then securely fastened between the tensile testing grips (covered in masking tape to improve gripping) and installed vertically in the Instron machine. The free end of the film was then mechanically lowered and secured into the mouth of the matching padded grips below it. Care was taken to

correctly align the fragile structures and several repeat measurements were taken to establish mean values.

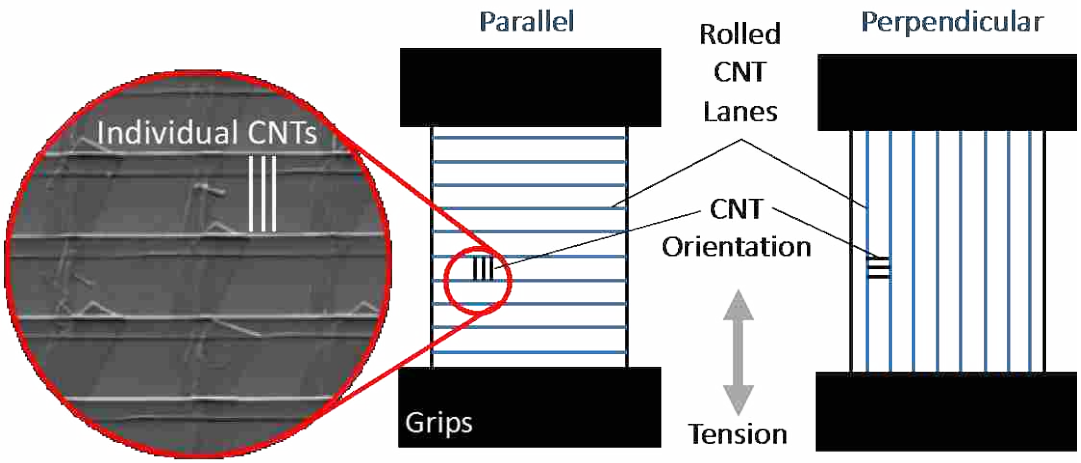

Figure 2-6. Tensile tests are performed in two film orientations; the films are placed in tension in a direction parallel with the rolled CNT fiber, or pulled perpendicular to the rolled CNT fiber.

After being secured, the films were pulled, until failure, at a rate of 5 μm per second with time, extension, and tension recorded throughout the test. The strain of the film was not directly measured with the Instron tests, as traditional methods of strain measurement are incompatible with the small size of thin films. Instead, strain was determined by dividing the measured extension of the Instron by the length of the film before elongation. From this data, and assuming there was no slippage, a stress-strain curve was generated and Young's modulus calculated.

2.3.3 Pressure Testing

Pressure testing was performed to quantify the ability of the carbon thin films to withstand a pressure differential across the film, and to determine the tensile strength and modulus of the material. Fabricated thin films were glued with M-Bond 610 strain gage adhesive to a 4 mm ID circular washer to allow for easy handling and positioning for testing (see also Figure 2-4). The sample was mounted over a 3 mm egress passage in a small pressure chamber with a viewport to monitor film deflection and failure (Figure 2-7).

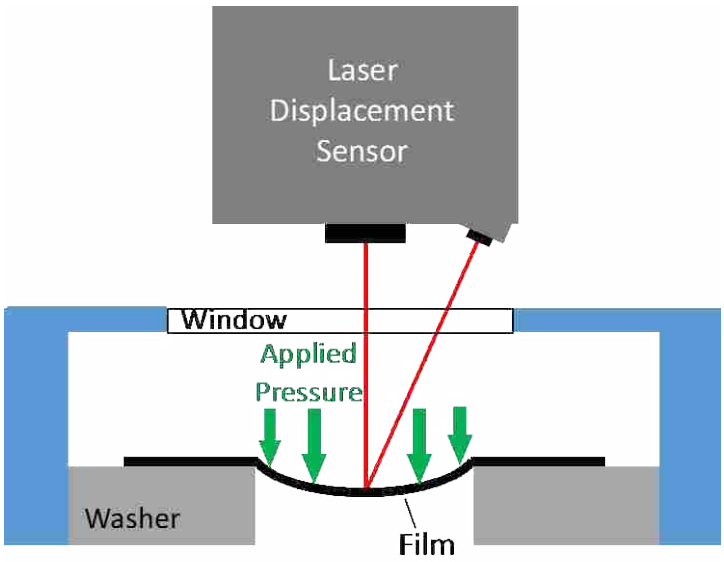

Figure 2-7. Schematic of the test setup for pressure testing used to indicate the differential pressure that could be sustained across the carbon thin films.

During pressure testing, the differential pressure to the film was applied in discrete steps with the bulge profile measured at each step with a Keyence LK-H052 laser displacement sensor. The sensor scanned a line across the film to measure the height change in the film at each

pressure. After each scan, the pressure was incrementally increased and the scanning process was repeated. Laser position, pressure, and gas flow were all recorded. The gas flow was used to determine if there were leaks in the film and to identify bursting conditions. A large drop in pressure with a corresponding increase in flow rate, along with an accompanying audible sound and visual confirmation, were used to identify the bursting condition.

The stress and strain of the material at each pressure step can be obtained with equations (2-4) and (2-5), taken from Vlassak using the measured displacement of the film [50-52]. By assuming the pressurized film takes the shape of a spherical cap and that both the stress and the strain are equi-biaxial, the relationship between pressure and deflection can be obtained for linear elastic membranes. The film deformation under pressure was fit with a 2nd order polynomial from the measured bulge profile data. The radius of the fitted circle can be used to calculate the stress (σ) in the film,

$$\sigma = \frac{P \cdot R_c}{2t} \tag{2-4}$$

where P is pressure, R_c is the radius of the fitted circle, and t is the thickness of the composite. Similarly, the strain of the film can be calculated as below,

$$\varepsilon = \frac{\sin^{-1}\left(\frac{r_0}{R_c}\right) - \frac{r_0}{R_c}}{\frac{r_0}{R_c}} \tag{2-5}$$

where ε is the strain and r_0 is the inner radius of the washers ($r_0 = 2$ mm).

Using equations (2-4) and (2-5), a stress vs strain plot was obtained with the slope of this curve yielding the biaxial modulus (Y). Young's modulus (E) is related to the biaxial modulus by equation (2-6).

$$E = Y(1-\nu) \tag{2-6}$$

where ν is Poisson's ratio. Young's modulus was acquired with traditional tensile testing (section 2.3.2) and Poisson's ratio was then estimated using this equation.

2.4 CNT Film Results

2.4.1 Surface Roughness Results

Results from optical profilometer scans for the top surface of the carbon thin film are shown in Figure 2-9. Top and bottom surfaces of the material were uniquely different as indicated by the roughness parameters in Table 2-2. Figure 2-9a shows the top surface, near the center of the rolled film, with a dramatic change in height along the line scan representing transition from row to row of rolled CNTs. The vertical lines observed in the SEM inset indicate overlapping rows of CNTs. From the film's thinnest point, the thickness increases by as much as 3 μm as the CNT rows overlap.

Figure 2-9b depicts a similar cross-plane profilometer scan over the final row of rolled CNTs at the edge of the film. This final row of CNTs (a solitary, uncompounded layer) is among the thinnest sections of the film. The film is approximately 1 μm thick in this region and increases to 3 μm with the additional neighboring row layered on top of it. SEM images indicate that the film thickness remains below approximately 5 μm, considerably thinner than the original CNT lane width of 10 μm. A profilometer scan normal to the direction of rolling is shown in Figure 2-9c. This orientation includes the horizontal bridging structures connecting neighboring CNT lanes, incorporated to facilitate vertical growth of the lanes across the entire surface. In

these regions where the bridging structures are rolled and collapse, the height variation increases approximately 3 μm with little variation in film thickness between the horizontal bridges.

The bottom surface of the thin film has none of the step changes associated with the top surface. Instead, it appears as simply a smooth sheet of amorphous carbon. A side-by-side comparison of the top and bottom surface can be seen below in Figure 2-8a and b, respectively. The darker regions shown in Figure 2-8b indicate where the iron pattern was originally present to grow the CNTs.

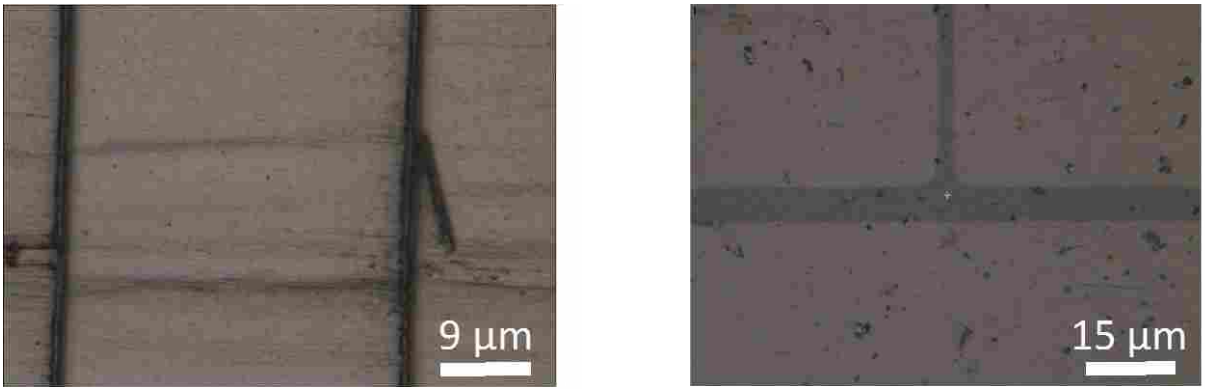

(a) (b)

Figure 2-8. (a) Top and (b) bottom surface regions where roughness measurements and profilometer scans were performed. The top, rougher surface of the film shows three stacked rows and a collapsed CNT bridge. The smoother, bottom side of the film, shows remnants of the iron pattern for growth.

Top and bottom surfaces were analyzed with the profilometer to determine surface roughness, seen in Table 2-2. The region of the bottom surface used for roughness calculations was a 70 μm x 90 μm area representative of the entire surface. This was the largest possible area

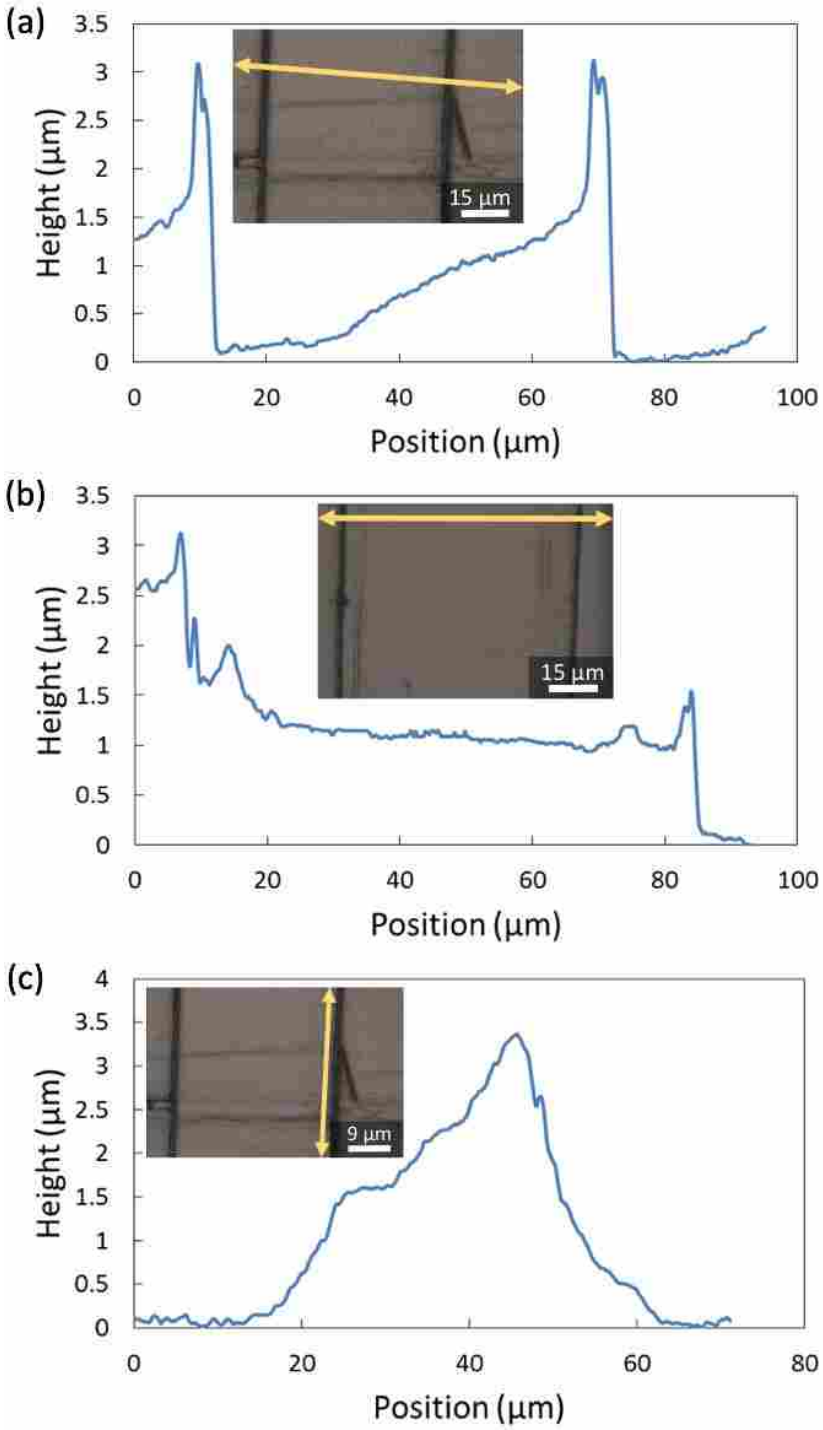

Figure 2-9. Profilometer scans indicating height variations on the top surface of the film for: (a) a region with three layers CNT lanes near the center of the rolled film; (b) a region near the edge of the film where only one or two layers of CNT lanes are present; (c) a region near the center of the rolled film where the horizontal bridging structures have collapsed.

for the aperture used. For the top surface, we analyzed a 50 μm x 50 μm region between the overlapping row, excluding the ridges. For the bottom surface, the arithmetic mean height is 0.05 μm, compared to a much rougher 0.86 μm for the top, and a root mean square height of 0.06 and 1.09 μm, respectively. Additionally, the variance in height along the top surface of the film is much greater than that observed for the bottom (Spvtop = 6.39 μm versus Spvbot 0.73 μm). For the bottom surface, the skewness is -0.13, which indicates that the height distribution is not quite normal, but is skewed a little above the mean plane (there are more valley features than peaks). However, the kurtosis is high at 4.40, which means despite the slight predominance of valley features, the peaks that are present are generally sharp. With a skewness and kurtosis of 0.95 and 3.75, respectively, the top surface is skewed more strongly below the mean plane (indicating more peaks than valleys) but with peaks that are less spiky than the bottom surface.

Table 2-2. Surface roughness measurements for the top and bottom sides of a thin film. The bottom side is the surface attached to the substrate during growth and is considerably more smooth, while the top surface is exposed during fabrication.

Variable	*Roughness Parameter*	*Top (Rough)*	*Bottom (Smooth)*
Sa	Arithmetic Mean Height (μm)	0.86	0.05
Sq	Root Mean Square Height (μm)	1.09	0.06
Sp	Maximum Peak Height (μm)	4.57	0.43
Sv	Maximum Valley Height (μm)	1.81	0.3
Spv	Peak-to-Valley Roughness (μm)	6.39	0.73
Ssk	Skewness	0.95	-0.13
Sku	Kurtosis	3.75	4.40

2.4.2 Tensile Testing Results

Tensile test results were acquired for 15 samples pulled in the aligned direction of the CNTs (8 samples) and in the transverse direction (7 samples; see also Figure 2-6). Variation in the results for a given orientation was observed, likely due to the manual fabrication and rolling of each film. However, the shape of each stress-strain curve was predominantly similar to the sample case shown in Figure 2-10. Stress was obtained using the load cell measurements and the film's cross-sectional area (3.3 mm by 3 μm). A 3 μm measurement was used as profilometer and SEM measurements indicated this was the film thickness in the thinnest region and, therefore, most likely the failure point. The film exhibits nonlinear behavior for much of the test. This is believed to be due to the fibrous, partially aligned nature of the material. As the film is pulled, tangled CNTs likely begin to stretch apart and experience increasing tension at different rates until they can be stretched no further. After the initial stretching, the stress-strain curve then becomes more linear, typically when the film was pulled past 70% of the max film stress. To consistently capture the slope of the linear region and the Young's modulus of the material, the linear region was determined to be where the film had experienced between 80% and 90% of the maximum tensile stress, as indicated by the red segment in Figure 2-10. This approach was applied to films with CNTs aligned parallel to the direction of tension as well as those aligned perpendicularly and is intended to avoid the "toe region," which is the initial non-linear relationship of the stress-strain curve found in fibrous materials, caused by fibers getting straightened and stretched [53, 54].

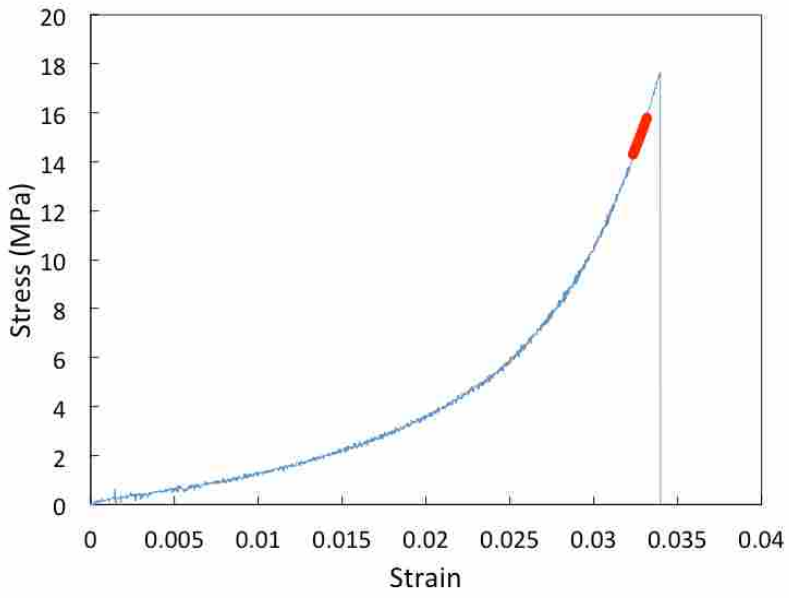

Figure 2-10. Sample stress-strain curve of a thin film under tension. The red segment was used as the linear region for determining the elastic modulus and is the stress captured between 80% and 90% of the max peak stress.

Results for all tensile tests on the thin films are shown in Table 2-3 below. The average peak stress for the films with nanotubes aligned parallel to the direction of tension (14.5 MPa) was observed to be greater than the films aligned perpendicularly (6.04 MPa). This was anticipated, as carbon nanotubes are strongest in tension. Despite the disparity in peak stress, the difference in the average modulus of elasticity for the two directions of tension was only approximately 15% (1402.7 MPa for aligned fibers and 1195.7 MPa for perpendicular). This similarity in the average modulus for the two orientations indicates (1) that although the film may not be perfectly isotropic, use of the biaxial modulus as an approximate calculation is appropriate and (2) the mechanical properties may be driven by the infiltration material and not by the CNTs. Though the standard deviation is large, this is not unexpected with fragile thin films and manual testing processes.

Table 2-3. Tensile test results for films with tension oriented both parallel and perpendicular (Figure 2-6) to the rolled CNTs. Peak stress is the stress at failure.

Orientation	*Sample #*	*Peak Stress (MPa)*	*E (MPa)*	*Avg. Peak Stress (MPa) [StDev]*	*Avg. E (MPa) [StDev]*
Aligned	1	5.86	424.6	14.5 [10.42]	1402.7 [1079.30]
	2	12.84	1074.7		
	3	15.73	2796.6		
	4	38.77	3294.9		
	5	17.66	1869.3		
	6	6.32	224.8		
	7	3.38	367.6		
	8	15.1	1168.9		
Perpendicular	1	9.63	815	6.04 [2.73]	1195.7 [1004.1]
	2	8.67	650.8		
	3	4.03	1245.7		
	4	8.57	3507.4		
	5	2.17	875.5		
	6	3.44	115.9		
	7	5.78	1159.6		

2.4.3 Pressure Testing Results

As described previously, films glued to 4 mm ID washers were placed under differential pressure until burst occurred. Bursting was confirmed by several methods. When the films burst, there was an auditory signal (a discernable "pop" sound) followed by the sound of increased gas flow in the test apparatus. The film failure was confirmed visually, as a camera mounted to the apparatus was used to record a picture at the start of each pressure step, capturing when the films burst. Figure 2-11 shows sequential images of a film bursting between pressure steps at 31 kPa (4.5 psi) and 32.75 kPa (4.75 psi). Finally, failure was also experimentally measured as the gas flow rate was recorded concurrent with incrementing pressure. When a film

bursts, a sudden increase in flow and a concurrent drop in differential pressure indicate that the film has failed, as seen in Figure 2-12.

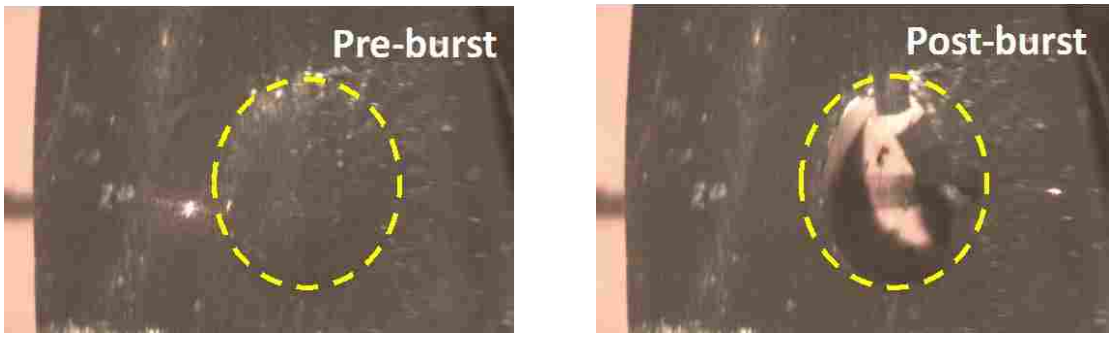

(a) (b)

Figure 2-11. Before (a) and after (b) a sample burst event at the transition from 31 kPa to 32.75 kPa.

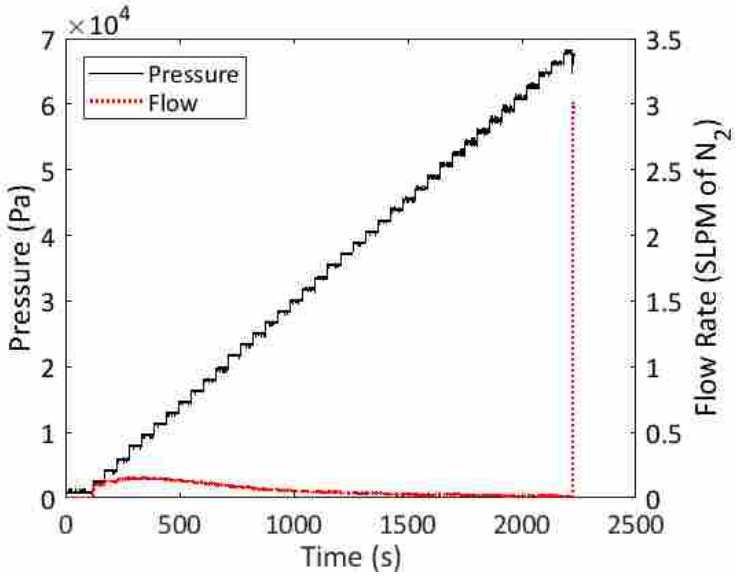

Figure 2-12. Pressure and flow rate for a film that burst at 67.2 kPa. Pressure was increased in quarter psi (1.72 kPa) steps until bursting, indicated by the surge seen in the nitrogen flow rate.

A bulge height profile measurement was taken with a laser at each pressure increment. Using the last measurement before bursting, a 2nd-order polynomial can be fit to the cluster of height data points to approximate the bulge shape. A 95% confidence interval is also plotted, as seen in Figure 2-13a. Using the maximum deflection before burst and the 95% confidence interval for each successful pressure test, we obtained an average maximum deflection just before burst of 182.8 µm for 16 films (see Figure 2-13b).

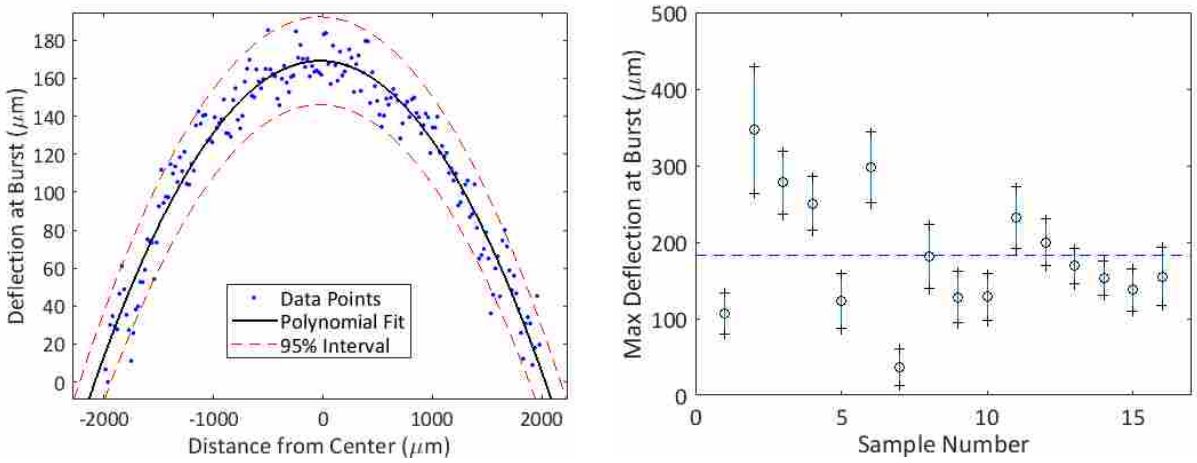

(a) (b)

Figure 2-13. (a) Deflection profile for a film just prior to burst at 68.9 kPa with a 2nd order polynomial fit and a 95% confidence interval of the deflection. (b) Maximum deflection just before burst based on the polynomial fit for 16 films with the 95% confidence interval included as error bars. The dashed line represents the average maximum deflection for the 16 films at 182.8 µm.

With a known washer inner radius of 2 mm, a circle can be superimposed using 3 data points – the max height, and 2 mm to either side of the origin. The radius of the circle can be

used with equations (2-4) through (2-6) to determine the stress and strain in the film at each pressure step. Plotting the stress-strain relationship, the slope obtained from these calculations yields the biaxial modulus (Figure 2-14).

Figure 2-14. Stress vs strain calculated from pressure test data for a film that burst at 82.7 kPa. The slope of the line fitted to the stress-stain curve represents the biaxial modulus.

The biaxial modulus was used to relate Young's modulus to Poisson's ratio for isotropic materials. The alignment of CNTs within the film may suggest anisotropic behavior. Tensile tests additionally indicated a somewhat anisotropic nature, but with a difference of only 15% in Young's modulus (section **Error! Reference source not found.**). However, the biaxial modulus may still be used to indicate the approximate behavior for Poisson's ratio using the average

Young's Modulus, especially if the infiltration of amorphous carbon is driving the mechanical properties.

Table 2-4 shows the biaxial modulus obtained for each pressure test, as well as the average among the tests (26.0 GPa). Due to the manual nature of the film production, the spread from these tests is large, with a standard deviation of 23.5 GPa. The resulting Poisson's ratio from the average biaxial modulus and Young's modulus is 0.95 (Eq. 6). Though this value for Poisson's ratio is large, CNT structures can have unusual Poisson's ratios, including negative ratios and values as large as 4.2 [55-58].

Table 2-4. Burst pressure, biaxial modulus, stress, and strain for each pressure test at failure with results organized by increasing burst pressure.

Sample Number	*Biaxial Modulus (GPa)*	*Pressure (kPa)*	*Stress (MPa)*	*Strain*
1	7.38	10.34	22.84	0.004
2	0.22	15.51	12.36	0.040
3	0.15	18.96	13.54	0.049
4	15.52	22.41	37.47	0.007
5	12.10	27.58	56.57	0.004
6	2.62	32.75	44.38	0.012
7	9.07	36.2	34.46	0.006
8	7.95	37.92	18.76	0.086
9	2.80	39.64	24.59	0.062
10	29.65	53.43	93.44	0.006
11	21.33	58.61	93.57	0.008
12	21.43	62.05	83.59	0.010
13	31.98	68.95	106.76	0.008
14	76.42	72.39	169.68	0.003
15	154.98	70.67	180.60	0.003
16	22.07	82.74	89.91	0.004
Average [StDev]	26.0 [39.2]	44.4 [22.8]	67.7 [52.7]	0.020 [0.025]

2.5 CNT Film Discussion

Just as carbon fiber materials have altered the landscape for a broad range of macroscopic structural applications, carbon nanotube structures have the potential to significantly improve the performance of microelectomechanical systems. Strength and durability is a highly sought-after trait for MEMS structures and devices. For the infiltrated carbon thin films created in this work, an average peak stress of 6.04 MPa was achieved in tension perpendicular to the rolled direction of the nanotubes, and 14.5 MPa parallel to the rolled CNTs. Though the average peak stress values are considerably weaker than the recorded 63 GPa tensile strength of individual CNT fibers [3], the strength of the film is sufficient to allow for handling and application in MEMs devices. Additional pressure testing revealed an average burst pressure of 44.4 kPa, with a max of 82.7 kPa, and an average biaxial modulus of 26.0 GPa. For reference, films that were fabricated the same way and then infiltrated with polymer forming a composite film had a strength times thickness of 242 N/m [59]. At approximately 6 μm, the resulting tensile strength for the CNT/polymer composite was 40.3 MPa, producing a stronger film as would be expected using polymer as a constituent instead of amorphous carbon.

Possible reasons for the reduction in strength relative to a single CNT are varied and unsurprising. The length of the individual fibers before being rolled was approximately 250 μm. When rolled laterally to create a 1 cm long film, the length of one of these fibers makes up only about 2.5% of the length of the sample. The mechanisms holding the film together are fiber entanglement, van der Walls forces, and carbon infiltration with amorphous carbon – all comparatively weak relative to the strength of the individual CNT fiber [60]. This weakness is

compounded due to the manual nature of the film's fabrication and testing, and the difficulty in detecting microdefects in the films – especially in tensile testing, where mounting films and aligning the direction of tension is paramount. Nevertheless, an entirely carbon sheet that provides transparency to some wavelengths of electromagnetic radiation remains attractive.

Many MEMS applications require smooth surfaces for optimal performance, often for optical or structural necessity. One side of the films created in this work is particularly smooth, with an arithmetic mean height and root mean square height of less than 0.06 μm, which opens the potential for subsequent microfabrication processing and use in MEMs or optical device applications requiring smooth surfaces. Profilometer scans confirmed a film thickness of 3 to 5 μm, and significantly different roughness scales for the top and bottom surfaces. The smoothest portion of the top (rougher) surface measured an arithmetic mean height of 0.86 μm and a root mean square height of 1.09 μm, though step height changes on the order of 1-3 μm were observed due to the overlapping layers.

Although a fibrous alignment of nanotubes may be indicative of anisotropic behavior, the porous nature of the film presents opportunities for infiltration of a secondary material to create a composite film. In this work, the carbon infiltration and Van der Waals forces may be the primary contributors for film integrity resulting in only a 15% difference observed in average Young's Modulus for both directions of tensile testing (1402.7 MPa parallel, 1195.7 MPa perpendicular). A similar work to integrate a polymer as a binder for a composite material has been published in a separate work [42].

2.6 CNT Film Conclusions

We have demonstrated a fabrication method for dense, aligned, CNT thin films on the order of 5 μm thick that is robust enough to physically handle without damage. A maximum peak stress of 38.77 MPa was measured in tension (aligned parallel to the rolled CNTs), with an average peak stress of 14.5 MPa and modulus of elasticity of 1402.7 MPa. For pressure testing, films could withstand a maximum differential pressure of 82.7 kPa (average of 44.4 kPa) before failure. The lower side of the film is particularly smooth, with an arithmetic mean height of just 0.05 μm, which opens possibilities for use in optical devices and other MEMs applications requiring smooth surfaces. As it is a film made from a base of nanotube fibers, it is expected that the material is not isotropic and would favor the direction of the fiber alignment, but our measurements indicate that the Young's modulus is in relative agreement for perpendicular and parallel alignments within approximately 15%. Variability inherent in manual processing of nanoscale features is a likely contributor to the large standard deviations observed in the measurements. With further exploration and experimentation, the film has potential for integration into a variety of MEMs devices.

3 THERMALLY INSULATING POROUS SILICA THIN FILM

3.1 Porous Silica Insulating Films Introduction

Single-walled carbon nanotubes (CNTs) are single-atom thick tubes of carbon with many incredible material properties. They have become a widely researched topic since the early 1990s [61] and have found their way into a variety of theoretical and practical applications. More recently, CNTS have become an invaluable material for use in many microeletromechanical systems (MEMS) due to their excellent mechanical, electrical, thermal, optical, chemical properties [1, 2, 62]. By using photolithographic methods, a vertically grown "forest" can be patterned into a desired shape or configuration. Using patterned carbon nanotubes as a scaffold, additional materials can be coated on or infiltrated into the forest, reinforcing the structure, in a process called carbon nanotube templated microfabrication (CNT-M) [28, 30, 63, 64]. The conditions and duration of an infiltration procedure can be controlled to result in highly dense or highly porous regions.

CNT-M has tremendous potential in creating insulating materials for MEMS sensors and provide either thermal or electrical isolation, including for gas chromatography (GC). GC is a technique used in analytical chemistry to separate and analyze volatile compounds and has been used in a wide range of fields, including forensic science; industrial, food, and environmental safety; biomedical research; and space exploration [65-67]. The premise of GC is to introduce a gas sample through a long channel to a detector at the exit, where constituents can be detected in

discrete separation bands at the channel exit. A major drawback of GC is the long column lengths necessary to achieve high-resolution separations making a MEMS-fabricated GC system impractical. However, by controlling the column thermal gradient, high-resolution separations can be achieved in shorter column lengths [68, 69]. Thermal gradient GC (TGGC) systems capable of high-resolution detection are possible assuming the necessary thermal gradients can be achieved. To date, micro-columns have been created in etched Si with thin film resistors as a heat source to initiate compound separation, with a small thermal conductivity detector for analysis [70, 71]. However, Si has a thermal conductivity that causes significant axial diffusion in the column as well as thermal cross-talk, which would significantly limit the ability of TGGC [72, 73]. A highly porous, low-conductivity material, like an aerogel, would increase the ability of a TGGC device to achieve high-resolution separation. Aerogels are lightweight, synthetic materials that can be fabricated from a variety of chemical compounds, including silica (SiO_2) [74], but attempts to incorporate them into small-scale sensors have failed to preserve the aerogel's low thermal conductivity [29]; furthermore, they generally lack structural integrity and do not have a clear path for integration into sensors. However, microfabricated thin layer chromatography plates can be created using silica-coated CNTs to improve insulation and maintain structural stability [30].

This work will explore the capabilities of CNTs as a framework for high-aspect-ratio MEMS fabrication by producing porous silica, insulating-thin-film for use as a thermal barrier in MEMS sensors and similar applications. CNT-M affords the method to create insulating thin films that can be integrated into MEMS/NEMS sensor architectures by infiltrating CNT forests with low pressure CVD (LPCVD) deposition of Si and then oxidizing at high temperatures to simultaneously burn out the carbon and oxidize the silicon. The result is a porous silica structure,

similar to an aerogel. This work explores the structurally stable, insulating thin-films created using CNTs scaffolds to achieve a porous insulating material and seeks to quantify the in-plane thermal conductivity using the concept of thermal resistance.

3.2 Porous Silica Fabrication and Testing Methods

3.2.1 Porous Silica Film Fabrication

The porous silica film is produced following the CNT-M procedure shown in Figure 3-1 with CNTs infiltrated using LPCVD. Although silicon, silicon oxide, and silicon nitride have all been investigated for use in infiltrating the CNT structure, silicon oxide has the lowest thermal conductivity. Additionally, it has the lowest coefficient of thermal expansion, so any large temperature changes experienced by silica structures are less likely to see major deformation.

The CNTs were grown, as in section 2.2.1, through a standard CVD process, flowing ethylene over a 4 nm iron catalyst on a silicon wafer separated by a 40 nm alumina diffusion layer (Figure 3-1a). The CNT forest used to form the silicon scaffolding was grown un-patterned and without undergoing any photolithographic process. In a 2.54 cm OD tube furnace, they were brought to 750°C while flowing 310 sccm of hydrogen (H_2) over them. At temperature, and while still flowing H_2, 340 sccm of ethylene (C_2H_4) was introduced for 50 seconds, growing CNTs 40 to 60 µm tall (50 µm average). After growth, the hydrogen and ethylene were turned off and Argon was flowed over the samples for 1 minute to allow the film to settle, and then the furnace was turned off while the Ar continued to cool the CNT forest. Once grown, CNTs were treated with ozone to improve silicon deposition [75]. Gas phase ozonation oxidizes the CNTs, which primes and increases the number of nucleation sites on the tubes and facilitates conformal

growth of silica along the CNT. To ozonate the CNTs, the O_3 gaseous reagent is simply passed over the forest with an Atlas 30 Ozone Generator (Absolute Ozone, Edmonton, Alberta) at an O_2 flow rate of 6.7 x 10^{-6} m^3/s with the current set at 45%, producing approximately 4.4 g/h of ozone. CNT samples were put into a 2.54 cm OD fused silica tube, purged for 1 min with oxygen, then exposed to the ozone flow for 45 minutes, before finally being purged again with 1 min of oxygen and then removed.

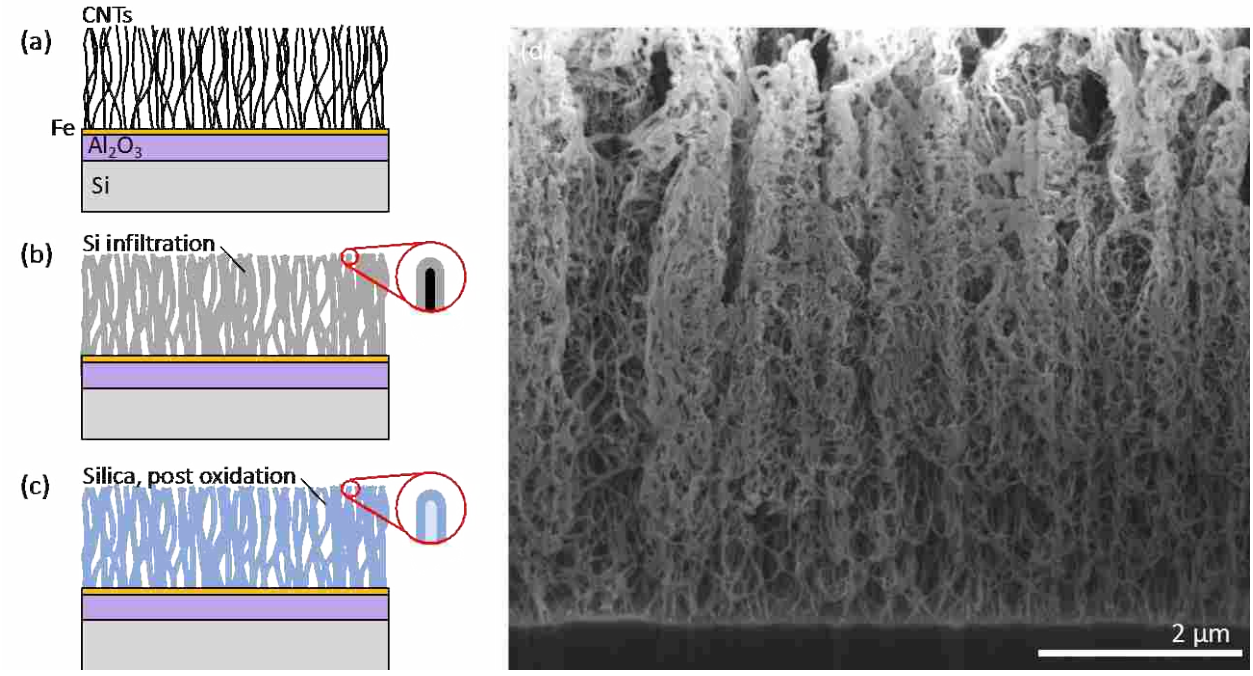

Figure 3-1. a) Vertically aligned CNTs (VACNTs) grown using lithographically patterned catalyst. b) Uniform Si infiltration of the CNT forest using LPCVD. c) Oxidation in an oxygen-rich furnace, burning away the CNTs and leaving a d) porous silica nanotube structure.

After CNTs were grown to the desired height and ozone treated, they were coated in silicon through a LPCVD method. Silicon deposition occurs in a high-temperature, low-pressure furnace (Figure 3-1b). The CNT samples were placed in a sealed furnace tube and are vacuum pumped down to $2x10^{-4}$ Torr. Once this pressure is reached, the remaining air in the furnace is purged from the tube by flowing nitrogen for 30 s. The purging of air prevents the combustion of CNTs that would occur at high temperatures. The nitrogen flowrate is then slowly reduced and then held constant as the pressure returns to $2x10^{-4}$ Torr. The furnace is then heated to 535 °C and the N_2 is turned off and replaced with the same flowrate of silane (H_4Si) for 15 minutes, keeping pressure at 200 mTorr. The silane is then turned off and the temperature is reduced to room temperature. When the temperature drops below 150 °C, the system is flushed with N_2 for one min. The vacuum pump can be turned off and N_2 can be introduced into the system until the pressure exceeds 500 mTorr, at which point the nitrogen can be turned off and the furnace tube seal can be broken to reintroduce atmosphere.

At this stage, the CNTs have been conformally coated with silicon. To burnout the carbon and convert the silicon to an insulating silicon dioxide, the films are placed in a furnace and heated to 850 °C in ambient air for 2 minutes, allowing the Si to oxidize (Figure 3-1c). When the samples are allowed to cool, the porous silica thin films are complete and can be used for testing. Samples of approximately a 1 – 4 cm^2 area were used for testing.

3.2.2 Density and Surface Roughness

The density of the porous silica film was determined by removing completed samples from the substrate and weighing its mass. The film was removed by scraping the surface to remove the silica, which was made easy by the brittle nature of the material. The volume of the film was

determined from the base area of the growth substrate and the measured height of the film. Dividing the mass of the film by its volume, the density of the porous silica films was obtained.

Surface roughness is an important feature for MEMs devices. A smooth SiO_2 structure can enable subsequent microfabrication steps for the creation and patterning of other microstructures. To measure the surface roughness, a Zeta Instruments 20 optical profilometer was used to image and analyze the surface features of several SiO_2 films (see also section 2.3.1). Optical profilometers can be used to create a 3D composite image of a sample, which can be analyzed with software to acquire a range of metrological data.

The optical profilometer takes initial measurements much like a normal microscope. There are various objective lenses that can be used to optically focus on the film surface, depending on the desired magnification and resolution. When focus is achieved, the profilometer creates a composite image from a series of scans in a range of focal lengths and then uses software to calculate various measurements. Using a large objective lens (100x), the optical profilometer was used to measure the surface roughness of the SiO_2 thin film.

3.2.3 Thermal Characterization

As a governing parameter in the conduction of thermal energy, the thermal conductivity of the porous oxide thin-film was measured. One-dimensional heat transfer was established and the thermal resistance across the thin-film was determined with the aid of a reference measurement. The layers of material present in the test condition and the associated thermal resistance for each layer is shown in Figure 3-3 (with the thermal resistance associated with the porous silica film highlighted in blue, Figure 3-3d).

To heat the silicon substrate to steady state and establish 1D heat transfer, samples were placed on a 5.1 x 2.5 x 1.3 cm copper block to act as a large, isothermal substrate that was heated by an attached thin-film heater. Four T-type thermocouples were placed in the copper block 0.64 cm from each side edge, and 1.52 and 0.64 cm from the top surface, embedded half way into the block to ensure isothermal conditions in the copper. Thermal insulating foam encased the sides and bottom of the copper block and heater to reduce heat loss and further ensure isothermal conditions, as seen in Figure 3-2. Test samples were placed on top of the isothermal copper block and heated via conduction.

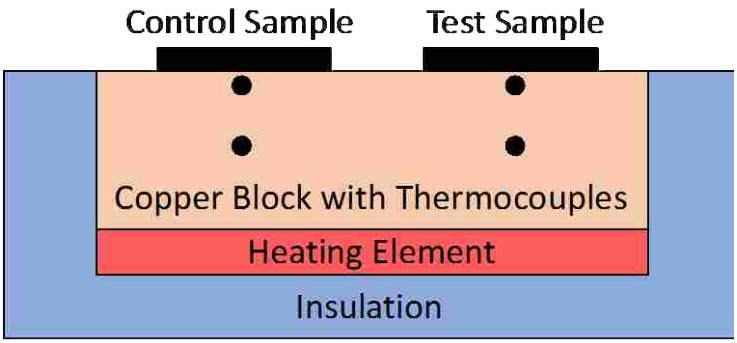

Figure 3-2. A heating element heats an insulated copper block equipped with four thermocouples. Samples with porous silica films can be compared directly to control samples without the porous silica film to determine the thermal conductivity of the insulating film.

During testing, a reference sample and one or more test samples were placed on a heated copper substrate, painted black in regions where the test samples were not located (Figure 3-3). The black paint (emissivity = 0.97, Krylon Ultra Flat Black) enabled use of an IR camera (FLIR SC6103) to measure surface temperatures. The top of each test sample (or reference or

benchmark sample) was also painted black in the same manner in order to determine the temperature difference across test samples (ΔT_{test}) during heating with the infrared temperature measurement. Each film was sprayed twice by hand with a smooth, even pass. Each pass lasted approximately 0.5 s over the 1 cm length of film. Control and benchmark samples were prepared in the same way. The surface temperature for each test was determined using an average over the area of the sample top surface.

Each test configuration (Figure 3-3a-c) was placed in a vacuum chamber (measuring 70 cm in diameter and 76.2 cm in length) and pumped down to a pressure of $<4x10^{-5}$ Torr in order to neglect convective heat transfer from the surface [76]. The IR camera was located exterior to the vacuum chamber with a direct line of sight to the sample surfaces through a 7.5 cm diameter sapphire window. The window had a band transmissivity of 0.81 – 0.85 for source temperatures between 323 K and 423 K in the spectral band of 3 – 5 μm, corresponding the wavelength range of measurement by the IR camera [77].

For thin samples (test and reference samples of thickness <600 μm), heat loss from the sides of the samples was neglected, resulting in 1D conduction heat transfer through the sample thickness. The thermal resistances in the stack are identified by each layer comprising the sample (Figure 3-3), namely: Si substrate (R_{Si}), alumina diffusion barrier (R_{al}), Fe catalyst (R_{Fe}), porous silica (R_{ps}) and the black paint (R_p). The conduction resistance for these layers can each be calculated using R = L/kA, assuming 1D, steady state conduction and constant properties (where L is the thickness, k is the thermal conductivity, and A is the area of each layer). An additional contact resistance (R_c) is present and includes the thermal grease used for good contact between substrate and sample.

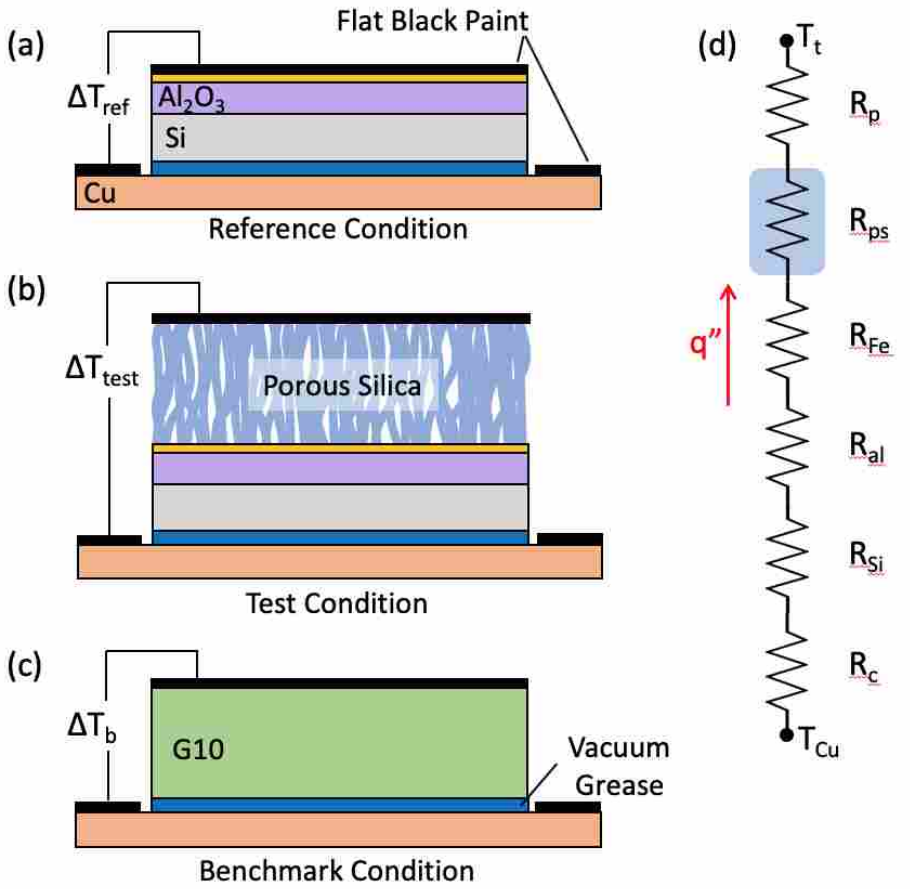

Figure 3-3. (a) Schematic of reference conditions used to determine the thermal resistance of all layers except the porous silica film. (b) Schematic of test condition used to determine the thermal resistance of the porous silica film. (c) Schematic of benchmark condition using a material of known thermal conductivity (G10) to confirm the measurement method. (d) Resistance network for the material stack for the test condition, including the porous silica film.

The reference test, which excludes the resistance associated with the porous silica film, can be used to determine a composite resistance associated with all other layers and the contact resistance combined, creating R_{comp}, equation (3-1).

$$R_{Comp} = R_c + R_{Si} + R_{al} + R_{Fe} + R_p \tag{3-1}$$

This composite resistance can be determined by measuring the temperature difference across the reference sample (ΔT_{ref}) and calculating the radiative heat rate leaving the surface of the reference sample, as given in equation (3-2).

$$q_{comp} = \frac{\Delta T_{ref}}{R_{comp}} \tag{3-2}$$

This heat rate (q_{comp}) is equivalent to the net radiative heat transfer rate shown in equation (3-3) since the heated surfaces are small relative to the isothermal vacuum chamber (T_{surr} = 296.15 K), as measured by a thermocouple placed on the aluminum chamber wall [78].

$$q_{rad} = \varepsilon \sigma A (T_t^4 - T_{surr}^4) \tag{3-3}$$

With q_{comp} and ΔT_{ref} obtained, the composite resistance is readily calculated and used to determine the resistance to heat transfer across the layers of material in the test condition excluding the resistance associated with the porous silica film.

A similar measurement as that outlined above for the reference condition is performed simultaneously for test surfaces that include a porous silica film, introducing an additional layer of resistance. With R_{comp} known from measurements associated with the reference condition, the rate of radiative heat loss (calculated using a new surface temperature T_1 for the test condition) can be equated to the measured ΔT_{test} divided by the sum of the composite resistance and the resistance associated with the porous silica film, yielding equation (3-4).

$$\varepsilon \sigma A (T_t^4 - T_{surr}^4) = \frac{\Delta T_{test}}{R_{comp} + R_{ps}} = \frac{\Delta T_{test}}{\frac{L_{comp}}{k_{comp} A} + \frac{L_{ps}}{k_{ps} A}} \tag{3-4}$$

The only unknown in equation (3-4) above is the through-plane thermal conductivity of the porous silica film (k_{ps}), which can now be obtained by inserting the known expression for the thermal conductivity of the composite, yielding equation (3-5).

$$k_{ps} = \frac{L_{ps}}{\frac{\Delta T_{test}}{\varepsilon\sigma(T_t^4 - T_{surr}^4)} - \frac{\Delta T_{ref}}{\varepsilon\sigma\left(T_{comp}^4 - T_{surr}^4\right)}} \tag{3-5}$$

T_t and T_{comp} are the top surface temperatures, read from the thermal camera, of the porous silica and the reference composite sample, respectively.

The copper block substrate temperature was increased by increasing the power dissipation in the thin-film heater using wire leads passing through a vacuum feedthrough until a desired temperature is reached. Each test was allowed to reach steady state behavior, defined as less than a 0.5 deg K temperature change in the copper block over 10 min. Repeat testing at several copper block temperatures was performed, with steady behavior reached for each condition. Testing in this manner allowed thermal conductivity measurement of the porous silica film over a range of temperatures. Higher copper block temperatures resulted in larger ΔT_{test} values and greater confidence in the temperature differences measured.

In order to verify the measurement approach for obtaining thermal conductivity, benchmark samples of Garolite fiberglass laminate (G10, McMaster-Carr) were cut from sheets of thickness 0.79, 1.59, and 3.18 mm. The 0.79 cm thick samples were used for the reference condition measurement with the 1.59 and 3.18 mm samples used as test condition samples following the approach outlined above for determining thermal conductivity for the porous silica film (Figure 3-3c). This approach of using both a thinner reference condition and a thicker test condition with G10, again allowed us to eliminate the requirement of obtaining an accurate

contact resistance measurement. In this manner, the thermal conductivity for G10 could be determined and compared with a published thermal conductivity value, thereby validating the measurement approach. Density and thermal conductivity of materials are summarized in Table 3-2.

3.3 Porous Silica Testing Results

3.3.1 Density and Surface Roughness Results

Measurements of density indicated that the porous silica film composition is similar to that of insulating silica aerogel. The volume for a 2 x 2 cm film grown to 15 μm tall film is 0.006 cm^3. A typical sample of this kind weighed 0.9 mg, resulting in a density of 0.15 g/cm^3. For comparison, the density of silica aerogel can range from 0.001 to 0.7 g/cm^3 [79]. The low density of the film is expected due its porous nature and is similar to aerogels; both are porous, silica-based insulators. The Si deposition successfully infiltrated the entire depth of the CNT forest, but the deposition was observed to be somewhat thicker at the top of the CNTs than at the base, as seen in Figure 3-1. The silica tubes, though thinner and sparser at the base of the film, remain intact and connected to the Si substrate. The thicker deposition rate at the top of the film appears to provide a smoother top surface.

The optical profilometer is a convenient tool to confirm the height of the thermal barrier film. Film height is shown in Figure 3-4, determined by measuring the height disparity between the substrate (revealed by scraping a small segment of the film) and film top surface. The film thickness is approximately 55 μm, which is approximately the same height as the CNT forest the film was formed from.

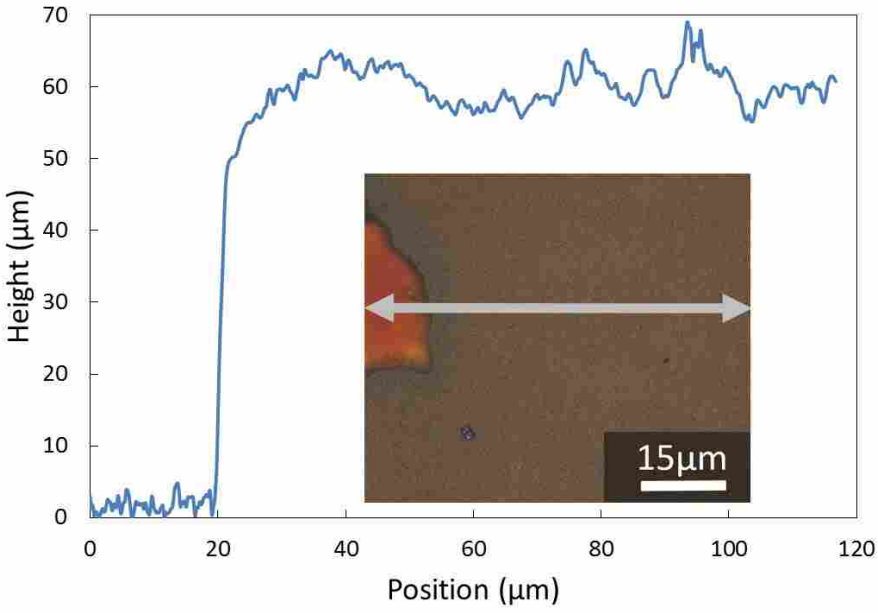

Figure 3-4. Profilometer scan of the top surface of a porous silica film indicating film height starting from an exposed region of the substrate and transitioning to the top of the film. Film thickness is approximately 55 µm.

The surface roughness of the porous silica film was determined using an optical profilometer interrogating an area of 70 µm x 90 (the largest available aperture area), representative of the entire top surface. Measurements that were taken include arithmetic mean (Sa), root mean square height (Sq), maximum peak and valley heights (Sp and Sv, respectively), distance between maximum peak and valley heights (Spv), skewness (Ssk), and kurtosis (Sku), as described in section 2.3.1. The results of the surface scans can be found in Table 3-1. The average arithmetic mean roughness (Sa) and root mean square roughness (Sq) of four tested films was 1.04 and 1.33 µm, respectively. Maximum peak height and valley height (Sp and Sv) are 4.93 µm and 5.62 µm, respectively, with a peak-to-valley roughness (Spv) of 10.55 µm. The skewness (Ssk) and kurtosis (Sku) of the top surface of the film was -0.08 and 3.67. A skewness of 0 indicates the average height of the peaks and valleys are equal, or symmetric. The film is relatively symmetric about the top plane, as indicated by the low skewness value. The porous

silica film is generally skewed evenly on average. A kurtosis value greater than 3 denotes that the surface peaks are more spikey than round; tested films indicate an Sku of 3.67.

Table 3-1. Surface roughness measurements for the top surface of the silica porous film, as measured by optical profilometer with a 100x magnification lens.

Sample #	*Sa (μm)*	*Sq (μm)*	*Sp (μm)*	*Sv (μm)*	*Spv (μm)*	*Ssk*	*Sku*
Sample 1	1.25	1.66	5.02	8.97	13.98	-0.85	4.95
Sample 2	1.12	1.42	5.68	4.64	10.32	0.02	3.20
Sample 3	0.97	1.22	5.09	5.00	10.09	0.27	3.22
Sample 4	0.80	1.01	3.94	3.88	7.81	0.23	3.32
Average	1.04	1.33	4.93	5.62	10.55	-0.08	3.67

3.3.2 Benchmark Test

Benchmark testing with G10 samples, using a thinner G10 sample as a reference condition, was used to ensure the measurement method provided correct results. Figure 3-5 indicates the measured thermal conductivity for two G10 samples of different thickness. The average thermal conductivity over the range of temperatures measured is 0.31 and 0.25 W m^{-1} K^{-1} for the 1.59 and 3.18 mm thick samples, respectively. Published values of the thermal conductivity for G10 are around 0.29 W m^{-1} K^{-1} [80]. Using this value as the correct thermal conductivity value, the current measurement approach for the two thicknesses provided results with an error of 7% and 14%. While additional refinements could be made to the measurement method, the good agreement between the measured and published thermal conductivity for G10, yields confidence in using the measurement method for obtaining reasonable thermal conductivity values for the porous silica films.

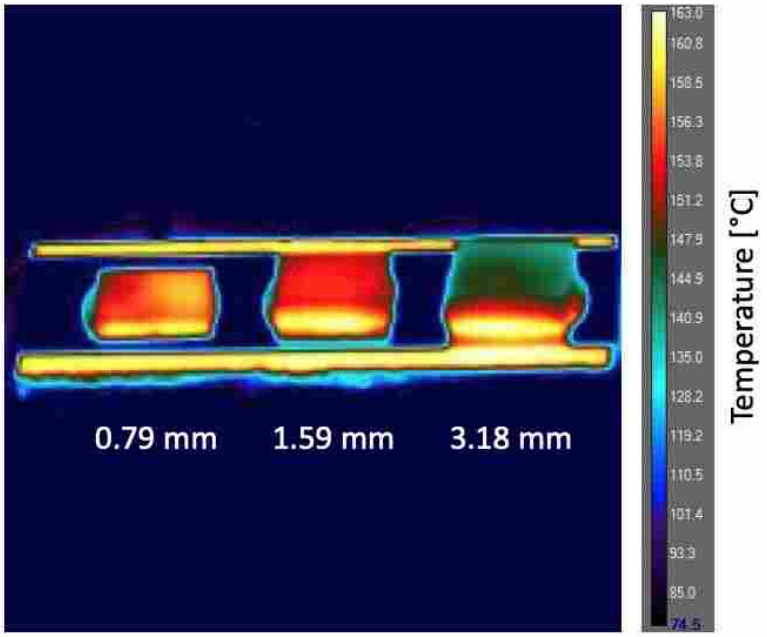

(a)

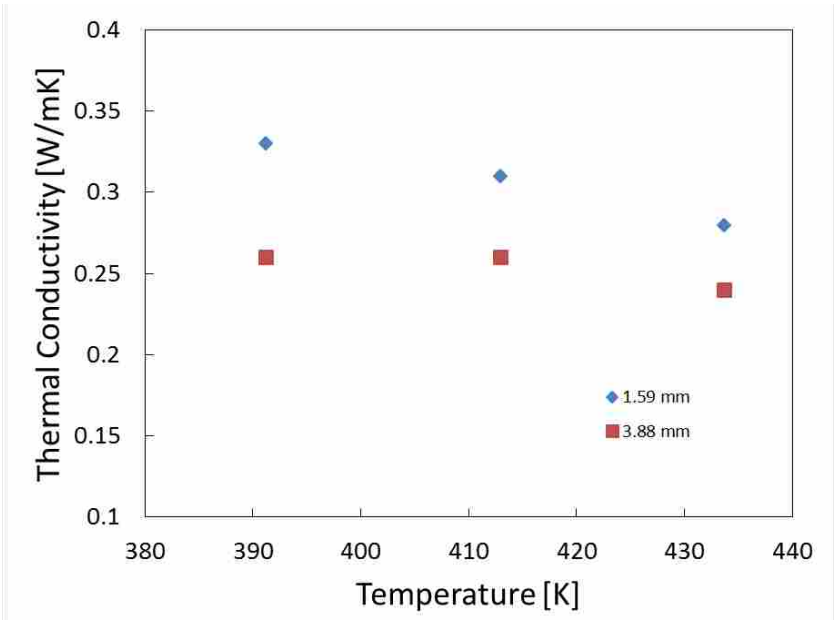

(b)

Figure 3-5. (a) Sample IR image of the benchmark testing indicating a cooler top surface temperature for a thicker G10 sample, corresponding to a higher sample resistance associated with increasing thickness. (b) Measured thermal conductivity for two benchmark samples (1.59 and 3.18 mm thick) obtained using the left sample (0.79 mm thick) as the reference condition at several copper substrate temperatures.

3.3.3 Porous Silica Thermal Conductivity

Thermal characterization of the porous silica films indicated a through-film thermal conductivity similar to silica aerogel. A representative thermal camera image with two reference samples and two porous silica samples placed on the copper substrate is shown in Figure 3-6.

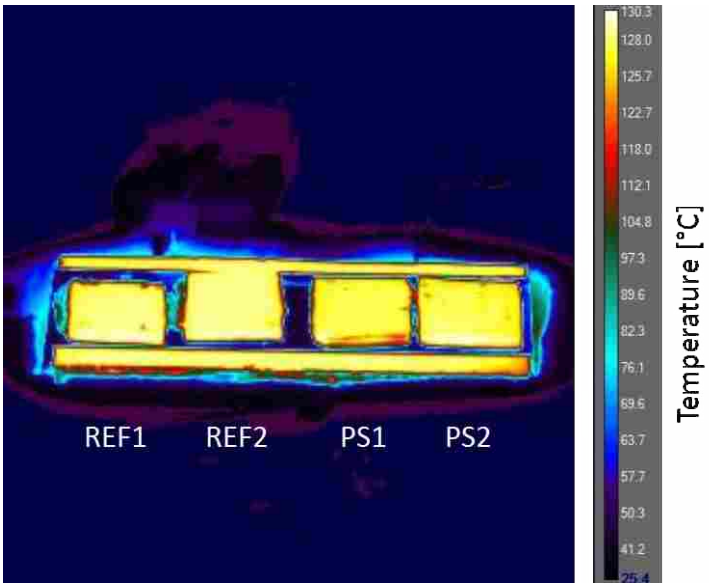

Figure 3-6. Sample temperature measurements for the experimental setup as observed through a sapphire viewing window. Samples labeled as PS1/PS2 and REF1/REF2 indicate samples with and without the porous silica film, respectively.

As the copper substrate increases in temperature, the porous silica and the control substrate sample also increase in temperature. However, the top surface of the insulating porous silica films increases slower than reference samples, as expected. The difference in temperature between a sample porous silica film and reference (ΔT_{test} - ΔT_{ref}), and the difference between a

sample porous silica film and copper substrate (ΔT_{test}), are shown in Figure 3-7. The temperature difference between samples with a porous silica film and reference samples (ΔT_{test} - ΔT_{ref}) becomes greater as the copper substrate temperature increases, but the increase appears linear, indicating a relatively constant thermal conductivity for the porous silica over the temperature range measured.

Based on the temperature measurements, including that reported in Figure 3-7a, the thermal conductivity of the porous silica films were determined using equation (3-5). Thermal conductivity for two porous silica films are shown in Figure 3-7b (PS1/PS2), obtained using two reference samples (REF1/REF2). The resulting four measurements obtained from a combination of different samples and references vary $\lesssim$15% relative to the mean at a given substrate temperature with a mean of 0.062 W/m·K over the range of 378 – 422 K. The thermal conductivity of the porous silica films seems to increase only slightly with increasing copper substrate temperature over the range of temperatures tested with a max spread of 0.054 – 0.071 over all measurements.

To contrast these values with relevant substances, Table 3-2 shows a comparison of density and thermal conductivities for several related materials, including silica aerogel, bulk silicon, and bulk silico dioxide. These results indicate that the thermal conductivity obtained for the porous silica thin films created and characterized using the methods proposed here are consistent with silica aerogels, while also offering a method for successful integration on a silicon platform.

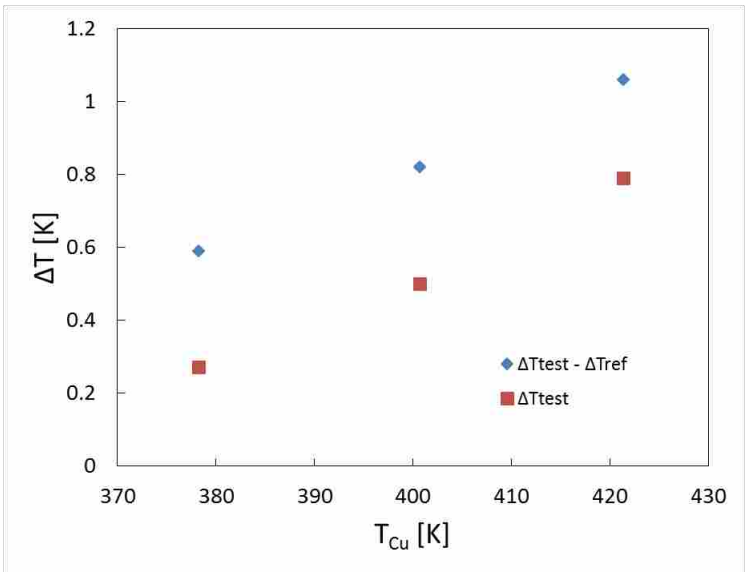

(a)

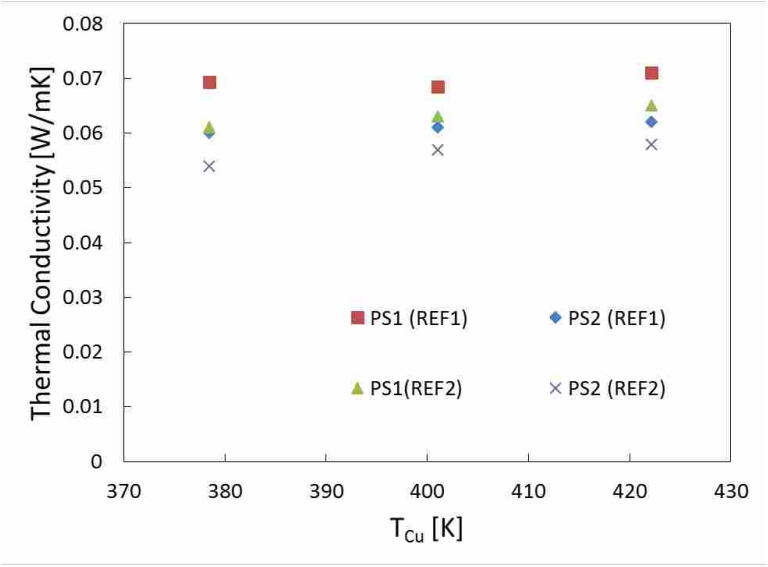

(b)

Figure 3-7. (a) Temperature difference between a sample porous silica film and reference (ΔT_{test} - ΔT_{ref}) and between a sample porous silica film and copper substrate (ΔT_{test}); both indicating a relatively linear increase. (b) Thermal conductivity results of two porous silica films (PS1/PS2) when compared to two separate control samples (REF1/REF2). A condition of "PS1 (REF1)" indicates a result for porous silica film 1 (PS1) relative to reference sample 1 (REF1).

Table 3-2. Density and thermal conductivity of several comparable or constituent materials for the porous silica [79, 81], and the porous silica itself.

Material	*Density (g/cm^3)*	*Thermal Conductivity ($W/m \cdot K$)*
Air	0.001	0.024
G10	1.800	0.290
Silicon	2.329	150.0
Silicon Dioxide	2.196	1.400
Silica Aerogel	0.001 - 0.700	0.004 - 0.030
Porous Silica	0.150	0.054 - 0.071

To better understand these results, the uncertainty in the measured thermal conductivity was also calculated. To calculate uncertainty, the partial derivative of each variable in equation (3-5) and the associated uncertainty of that variable were used, as in equation (3-6).

$$U_k = \left[\left(\frac{\partial k}{\partial L_{ps}}\right)^2 {U_{L_{ps}}}^2 + \left(\frac{\partial k}{\partial T_{cu}}\right)^2 {U_{T_{cu}}}^2 + \left(\frac{\partial k}{\partial T_t}\right)^2 {U_{T_t}}^2 + \left(\frac{\partial k}{\partial T_{comp}}\right)^2 {U_{T_{comp}}}^2 + \left(\frac{\partial k}{\partial T_{surr}}\right)^2 {U_{T_{surr}}}^2 + \left(\frac{\partial k}{\partial \varepsilon}\right)^2 {U_\varepsilon}^2\right]^{1/2} \quad (3\text{-}6)$$

The uncertainty of the thickness of the film was observed to be about 10% of the total film thickness based on SEM measurements and scratch tests with the optical profilometer. Emissivity uncertainty is taken to be the uncertainty of the intrinsic emissivity reflectometer measurement (±0.006). The uncertainty of T_{surr} is the uncertainty of a T-type thermocouple (±1 K), while the uncertainty of the remaining temperature readings, all taken by thermal camera, was obtained from manufacturer specifications indicating a 2% variation in the temperature value [77]. Using these values, the total uncertainty of the porous silica conductivity is 0.32

W/m·K, dominated primarily by the uncertainty in thermal camera temperature readings. At a maximum measured conductivity of 0.071 W/m·K, the uncertainty range becomes 0 to 0.391 W/m·K, which is large but still well below the conductivity of bulk silicon dioxide, 1.4 W/m·K.

Alternatively, because equation (3-5) is interested more in the relative temperature of the porous silica and reference sample rather than the absolute temperature, and since we can assume any error in thermal camera temperature measurements will work in the same direction for both the silica and reference samples, we can treat ΔT_{test} and ΔT_{ref} as single variable and can use equation (3-7) to calculate uncertainty instead.

$$U_k = \left[\left(\frac{\partial k}{\partial L_{ps}}\right)^2 {U_{L_{ps}}}^2 + \left(\frac{\partial k}{\partial \Delta T_{test}}\right)^2 {U_{\Delta T_{test}}}^2 + \left(\frac{\partial k}{\partial T_t}\right)^2 {U_{T_t}}^2 + \left(\frac{\partial k}{\partial T_{comp}}\right)^2 {U_{T_{comp}}}^2 \right. \\ \left. + \left(\frac{\partial k}{\partial T_{surr}}\right)^2 {U_{T_{surr}}}^2 + \left(\frac{\partial k}{\partial \Delta T_{ref}}\right)^2 {U_{\Delta T_{ref}}}^2 + \left(\frac{\partial k}{\partial \varepsilon}\right)^2 {U_\varepsilon}^2 \right]^{1/2} \quad (3\text{-}7)$$

Using the same uncertainty values as before, and using the 2% camera measurement uncertainty for ΔT_{ref} and ΔT_{test}, the total uncertainty becomes 0.0075 W/m·K. With this uncertainty, the conductivity range of 0.054-0.071 W/m·K becomes 0.047-0.079 W/m·K.

3.4 Porous Silica Discussion

Density measurements taken were from a 2 x 2 cm film grown to 15 μm tall film. Though this is shorter than most of our porous silica samples, the silicon LPCVD deposition rate was observed to be relatively conformal. The silicon deposition thickness is similar near the top and bottom of the film, with a somewhat thicker deposition near the top. It is likely that the 15 μm tall film will have a somewhat thicker LPCVD Si deposition, and may have a denser film than the 50 μm tall porous silica films used for thermal conductivity testing. However, 0.15 g/cm^3 is

likely a reasonable approximation with any density variation due to film height still within the range of other silica aerogels (0.001 to 0.7 g/cm^3). As the current porous silica films and other aerogels are both made from the same material with comparable density, the similarities in thermal conductivity observed are expected.

Prior to using G10 as a benchmark test, an attempt was made at using stainless steel to validate the thermal conductivity test. These tests failed for several reasons. First, thicker samples of stainless steel were used than our other benchmark tests. For these tests to be effective, thermal bleeding out of the sides of the samples must be small, so the height of the film must be small relative to its square. The larger issue, however, was that the thermal conductivity of steel was much larger than G10. Because the samples were so conductive, temperature differences for different variations in thickness were hard to measure at the relatively low-temperature testing conditions used. This problem was resolved using less conductive G10.

In addition to the complications in benchmark testing, there were early obstacles getting consistent readings from the porous silica films. That was deemed to be from poor thermal contact between the copper substrate and the test samples. The films were originally placed loosely on the top of the block, held in place only by the weight of its own mass. The addition of thermal vacuum grease between the two materials alleviated this issue by promoting consistent thermal contact throughout the interface surfaces.

Thermal conductivity experiments were performed in a vacuum. It is worth considering how the film would react in atmosphere, theoretically. The thermal conductivity of the film in a vacuum is approximately 0.06 W/m·K, while the conductivity of air is 0.024 W/m·K [82]. So adding air may lower the films average thermal conductivity, assuming air infiltrates the cavities of the film. However, due to the Knudsen effect, the overall thermal conductivity may be even

further reduced [83]. The Knudsen effect occurs when a materials pore diameter is less than the mean free path of the gas molecules. Instead of colliding with other gas molecules, the molecules will instead collide ballistically with the pore walls. In air, this occurs in pores of diameter 40 nm and smaller, and can reduce the thermal conductivity to less than 0.004 W/m·K. Regions of the film certainly fall within this requirement, and the diameter of individual silica nanotubes has been measured by SEM to be as small as 6 nm in diameter, well below the threshold required for the Knudsen effect to occur.

The surface roughness of the porous silica was found to be 1.04 μm. Generally, the smoother a surface is, the more useful it is for integration into other MEMs applications. One possible mechanism for reducing the resulting surface roughness may be to spray CNTs on top of the vertically grown CNTs. Loose CNTs can be sonicated in a solvent and then sprayed using an airbrush to achieve this condition, changing the top plane from a surface of relatively rough vertically aligned CNTs to a surface made from smoother, horizontally aligned CNTs. The porous silica fabrication method can then continue unaltered to create a film with a smoother top surface [84]. Alternatively, Plasma Enhanced CVD (PECVD) can be used after LPCVD infiltration to cap the top surface of the film. While LPCVD infiltrates the whole CNT forest conformally and through to the bottom of the forest, PECVD coats CNTs thicker at the top of the fiber and caps off the top surface, potentially creating a smoother top surface [85].

3.5 Porous Silica Conclusion

This work reports on a testing method to determine the thermal conductivity of thin films with low conductivities and used to quantify the thermal conductivity of a porous silica film created using CNTs as a scaffold. The porous silica film may offer great potential in the realm

of MEMs structures as it has excellent thermally insulating properties, with a thermal conductivity of approximately 0.062 W/m·K in the range of 378 – 422 K. This thermal conductivity value is in the range of other silica aerogels and somewhat higher than air, but significantly lower than Si and bulk SiO_2. The material, as a porous film, also has a very low density of 0.15 g/cm^3. The film is also relatively smooth and flat, with an average arithmetic mean of 1.04 μm and a skewness of -0.08.

The conclusion of this work presents several opportunities for further exploration. To fully take advantage of the benefits of this new porous silica film, additional work may be done to examine the effect of film height and silica thickness over a potentially broader range of temperatures. Mechanical testing would reveal film strength for potential integration into MEMs. These films can be patterned with photolithography or by ion etching to make channels or other useful shapes, for use in gas chromatography systems or other MEMs devices and offers a method to minimize thermal crosstalk in MEMS structures without suspending structures.

4 CONCLUSION

We have demonstrated fabrication methods to create a freestanding, aligned carbon nanotube thin film. Additionally, we have utilized CNT templated microfabrication to create porous silica insulating thin film integrated into the base silicon substrate. Patterning CNTs with photolithography can create unique films and microstructures for use in a variety of applications. Furthermore, we have shown how effective CNTs can be as a scaffolding to create intricate and versatile microstructures when infiltrated with the appropriate material. These films have further potential for integration into MEMs devices and applications.

The carbon thin films have potential for use in portable x-ray technology. Handheld x-ray devices emit rays from an x-ray tube, kept under vacuum, for analysis. For improved resolution, the x-rays cannot be hindered by thick physical barriers. This requires a thin-film that will allow x-rays to pass through to the detector under vacuum, while also being strong enough to maintain the pressure differential present. Beryllium films are commonly used for x-ray windows, but they are expensive and toxic. A carbon thin film, reinforced by CNTs would be a strong, inexpensive alternative to current window technology.

We created a CNT carbon thin film less than 5 μm thick using a rolled CNT pattern as a structural base and then infiltrating voids in the mat with amorphous carbon. This film held nearly one atmosphere of pressure, so with an underlying support or grid structure, it may be sufficient to hold the pressure necessary to hold an x-ray detector under pressure. Additionally, unrecorded

tests showed these films shared a similar x-ray transmissivity profile to beryllium films, making them viable replacements. Further use of the film can be made by adding additional material with desired properties. Boyer et al. hot-pressed polymer into the film to create smooth, thin CNT composite sheets [42]. Using different infiltrating materials, new types of thin films with a CNT substructure can be created.

The porous silica material has great potential in all MEMs applications requiring insulating material. The porous silica exhibits excellent thermal insulation. Insulation is an essential component for many electrical systems, and can be hard to realize for many MEMs devices. A robust, well-insulating film can immediately improve the performance of many electrical mechanisms. The CNT forest used as a scaffolding can be patterned to create more intricate insulating structures, channels, and geometries, or the silica material can be etched away using methods like focus ion beam milling, allowing both bottom-up and top-down design. Surface roughness of the film can be further increased by utilizing sprayed CNTs and/or non-conformal PECVD to cap the top surface. We have showed that these films would make an excellent thermal barrier to make thermal gradient gas chromatography possible. The barrier can prevent thermal bleeding across the top surface, and patterned porous silica can be used to create insulated channels for gas chromatography.

As with the carbon thin films, the porous silica films demonstrate the ability for CNTs to be used as a structural template for microstructure fabrication. Also like the carbon films, porous silica films can be infiltrated with different materials besides silicon, opening interesting possibilities in material creation. This work has demonstrated the viability of using CNTs as a scaffolding for various microstructures. These applications open a wide range of possibilities for microscale architecture, and in creating designs, shapes, forms, and structures that were previously

impractical or otherwise impossible, to create increasingly smaller microelectromechanical systems.

REFERENCES

1. Charlier, J.-C., X. Blase, and S. Roche, *Electronic and transport properties of nanotubes.* Reviews of Modern Physics, 2007. **79**(2): p. 677-732.

2. Pop, E., D. Mann, Q. Wang, K. Goodson, and H. Dai, *Thermal Conductance of an Individual Single-Wall Carbon Nanotube above Room Temperature.* Nano Letters, 2006. **6**(1): p. 96-100.

3. Yu, M.-F., O. Lourie, M.J. Dyer, K. Moloni, T.F. Kelly, and R.S. Ruoff, *Strength and Breaking Mechanism of Multiwalled Carbon Nanotubes Under Tensile Load.* Science, 2000. **287**(5453): p. 637.

4. Ago, H., K. Petritsch, M.S.P. Shaffer, A.H. Windle, and R.H. Friend, *Composites of Carbon Nanotubes and Conjugated Polymers for Photovoltaic Devices.* Advanced Materials, 1999. **11**(15): p. 1281-1285.

5. Ivanov, I., A. Puretzky, G. Eres, H. Wang, Z. Pan, H. Cui, R. Jin, J. Howe, and D.B. Geohegan, *Fast and highly anisotropic thermal transport through vertically aligned carbon nanotube arrays.* Applied Physics Letters, 2006. **89**(22): p. 223110.

6. Vigolo, B., A. Pénicaud, C. Coulon, C. Sauder, R. Pailler, C. Journet, P. Bernier, and P. Poulin, *Macroscopic Fibers and Ribbons of Oriented Carbon Nanotubes.* Science, 2000. **290**(5495): p. 1331.

7. Ericson, L.M., H. Fan, H. Peng, V.A. Davis, W. Zhou, J. Sulpizio, Y. Wang, R. Booker, J. Vavro, C. Guthy, A.N.G. Parra-Vasquez, M.J. Kim, S. Ramesh, R.K. Saini, C. Kittrell, G. Lavin, H. Schmidt, W.W. Adams, W.E. Billups, M. Pasquali, W.-F. Hwang, R.H. Hauge, J.E. Fischer, and R.E. Smalley, *Macroscopic, Neat, Single-Walled Carbon Nanotube Fibers.* Science, 2004. **305**(5689): p. 1447.

8. Zhang, X., T.V. Sreekumar, T. Liu, and S. Kumar, *Properties and Structure of Nitric Acid Oxidized Single Wall Carbon Nanotube Films.* The Journal of Physical Chemistry B, 2004. **108**(42): p. 16435-16440.

9. Ajayan, P.M., L.S. Schadler, C. Giannaris, and A. Rubio, *Single-Walled Carbon Nanotube–Polymer Composites: Strength and Weakness.* Advanced Materials, 2000. **12**(10): p. 750-753.

10. Engel, M., J.P. Small, M. Steiner, M. Freitag, A.A. Green, M.C. Hersam, and P. Avouris, *Thin Film Nanotube Transistors Based on Self-Assembled, Aligned, Semiconducting Carbon Nanotube Arrays.* ACS Nano, 2008. **2**(12): p. 2445-2452.

11. Wang, X., Q. Li, J. Xie, Z. Jin, J. Wang, Y. Li, K. Jiang, and S. Fan, *Fabrication of Ultralong and Electrically Uniform Single-Walled Carbon Nanotubes on Clean Substrates.* Nano Letters, 2009. **9**(9): p. 3137-3141.

12. Kaempgen, M., C.K. Chan, J. Ma, Y. Cui, and G. Gruner, *Printable Thin Film Supercapacitors Using Single-Walled Carbon Nanotubes.* Nano Letters, 2009. **9**(5): p. 1872-1876.

13. Feng, C., K. Liu, J.-S. Wu, L. Liu, J.-S. Cheng, Y. Zhang, Y. Sun, Q. Li, S. Fan, and K. Jiang, *Flexible, Stretchable, Transparent Conducting Films Made from Superaligned Carbon Nanotubes.* Advanced Functional Materials, 2010. **20**(6): p. 885-891.

14. Yamada, T., N. Makiomoto, A. Sekiguchi, Y. Yamamoto, K. Kobashi, Y. Hayamizu, Y. Yomogida, H. Tanaka, H. Shima, H. Akinaga, D.N. Futaba, and K. Hata, *Hierarchical Three-Dimensional Layer-by-Layer Assembly of Carbon Nanotube Wafers for Integrated Nanoelectronic Devices.* Nano Letters, 2012. **12**(9): p. 4540-4545.

15. Ko, W.-Y. and K.-J. Lin, *Highly conductive, transparent flexible films based on metal nanoparticle-carbon nanotube composites.* J. Nanomaterials, 2013. **2013**: p. 10-10.

16. Rowell, M.W., M.A. Topinka, M.D. McGehee, H.-J. Prall, G. Dennler, N.S. Sariciftci, L. Hu, and G. Gruner, *Organic solar cells with carbon nanotube network electrodes.* Applied Physics Letters, 2006. **88**(23): p. 233506.

17. Zhang, M., S. Fang, A.A. Zakhidov, S.B. Lee, A.E. Aliev, C.D. Williams, K.R. Atkinson, and R.H. Baughman, *Strong, Transparent, Multifunctional, Carbon Nanotube Sheets.* Science, 2005. **309**(5738): p. 1215.

18. Munzer, A.M., M. Heimgreiter, K. Melzer, A. Weise, B. Fabel, A. Abdellah, P. Lugli, and G. Scarpa, *Back-gated spray-deposited carbon nanotube thin film transistors operated in electrolytic solutions: an assessment towards future biosensing applications.* Journal of Materials Chemistry B, 2013. **1**(31): p. 3797-3802.

19. Ding, S., S.R. Das, B.J. Brownlee, K. Parate, T.M. Davis, L.R. Stromberg, E.K.L. Chan, J. Katz, B.D. Iverson, and J.C. Claussen, *CIP2A immunosensor comprised of vertically-aligned carbon nanotube interdigitated electrodes towards point-of-care oral cancer screening.* Biosensors and Bioelectronics, 2018. **117**: p. 68-74.

20. Brownlee, B.J., K.M. Marr, J.C. Claussen, and B.D. Iverson, *Improving sensitivity of electrochemical sensors with convective transport in free-standing, carbon nanotube structures.* Sensors and Actuators B: Chemical, 2017. **246**: p. 20-28.

21. Liu, D., H. Wang, P. Du, and P. Liu, *Independently double-crosslinked carbon nanotubes/polyaniline composite films as flexible and robust free-standing electrodes for high-performance supercapacitors.* Carbon, 2017. **122**: p. 761-774.

22. Hyder, M.N., S.W. Lee, F.Ç. Cebeci, D.J. Schmidt, Y. Shao-Horn, and P.T. Hammond, *Layer-by-Layer Assembled Polyaniline Nanofiber/Multiwall Carbon Nanotube Thin Film Electrodes for High-Power and High-Energy Storage Applications.* ACS Nano, 2011. **5**(11): p. 8552-8561.

23. Wang, Y.F., N. Néel, J. Kröger, H. Vázquez, M. Brandbyge, B. Wang, and R. Berndt, *Voltage-dependent conductance states of a single-molecule junction.* Journal of Physics: Condensed Matter, 2012. **24**(39): p. 394012.

24. Wang, M., H. Chen, W. Lin, Z. Li, Q. Li, M. Chen, F. Meng, Y. Xing, Y. Yao, C.-p. Wong, and Q. Li, *Crack-Free and Scalable Transfer of Carbon Nanotube Arrays into Flexible and Highly Thermal Conductive Composite Film.* ACS Applied Materials & Interfaces, 2014. **6**(1): p. 539-544.

25. Gspann, T.S., S.M. Juckes, J.F. Niven, M.B. Johnson, J.A. Elliott, M.A. White, and A.H. Windle, *High thermal conductivities of carbon nanotube films and micro-fibres and their dependence on morphology.* Carbon, 2017. **114**: p. 160-168.

26. Hu, D., W. Gong, J. Di, D. Li, R. Li, W. Lu, B. Gu, B. Sun, and Q. Li, *Strong graphene-interlayered carbon nanotube films with high thermal conductivity.* Carbon, 2017. **118**: p. 659-665.

27. Zhong, G., J.H. Warner, M. Fouquet, A.W. Robertson, B. Chen, and J. Robertson, *Growth of Ultrahigh Density Single-Walled Carbon Nanotube Forests by Improved Catalyst Design.* ACS Nano, 2012. **6**(4): p. 2893-2903.

28. Song, J., D.S. Jensen, D.N. Hutchison, B. Turner, T. Wood, A. Dadson, M.A. Vail, M.R. Linford, R.R. Vanfleet, and R.C. Davis, *Carbon-Nanotube-Templated Microfabrication of Porous Silicon-Carbon Materials with Application to Chemical Separations.* Advanced Functional Materials, 2011. **21**(6): p. 1132-1139.

29. Harris, K.D., D. Vick, E.J. Gonzalez, T. Smy, K. Robbie, and M.J. Brett, *Porous thin films for thermal barrier coatings.* Surface and Coatings Technology, 2001. **138**(2): p. 185-191.

30. Jensen, D.S., S.S. Kanyal, V. Gupta, M.A. Vail, A.E. Dadson, M. Engelhard, R. Vanfleet, R.C. Davis, and M.R. Linford, *Stable, microfabricated thin layer chromatography plates without volume distortion on patterned, carbon and Al2O3-primed carbon nanotube forests.* Journal of Chromatography A, 2012. **1257**: p. 195-203.

31. Wang, Z., Z. Liang, B. Wang, C. Zhang, and L. Kramer, *Processing and property investigation of single-walled carbon nanotube (SWNT) buckypaper/epoxy resin matrix nanocomposites.* Composites Part A: Applied Science and Manufacturing, 2004. **35**(10): p. 1225-1232.

32. Wu, Z., Z. Chen, X. Du, J.M. Logan, J. Sippel, M. Nikolou, K. Kamaras, J.R. Reynolds, D.B. Tanner, A.F. Hebard, and A.G. Rinzler, *Transparent, Conductive Carbon Nanotube Films.* Science, 2004. **305**(5688): p. 1273.

33. Liu, Q., T. Fujigaya, H.-M. Cheng, and N. Nakashima, *Free-Standing Highly Conductive Transparent Ultrathin Single-Walled Carbon Nanotube Films.* Journal of the American Chemical Society, 2010. **132**(46): p. 16581-16586.

34. Ding, W., S. Pengcheng, L. Changhong, W. Wei, and F. Shoushan, *Highly oriented carbon nanotube papers made of aligned carbon nanotubes.* Nanotechnology, 2008. **19**(7): p. 075609.

35. Xu, W., Y. Chen, H. Zhan, and J.N. Wang, *High-Strength Carbon Nanotube Film from Improving Alignment and Densification.* Nano Letters, 2016. **16**(2): p. 946-952.

36. Bradford, P.D., X. Wang, H. Zhao, J.-P. Maria, Q. Jia, and Y.T. Zhu, *A novel approach to fabricate high volume fraction nanocomposites with long aligned carbon nanotubes.* Composites Science and Technology, 2010. **70**(13): p. 1980-1985.

37. Peng, B., M. Locascio, P. Zapol, S. Li, S.L. Mielke, G.C. Schatz, and H.D. Espinosa, *Measurements of near-ultimate strength for multiwalled carbon nanotubes and irradiation-induced crosslinking improvements.* Nature Nanotechnology, 2008. **3**: p. 626.

38. Yu, M.-F., B.S. Files, S. Arepalli, and R.S. Ruoff, *Tensile Loading of Ropes of Single Wall Carbon Nanotubes and their Mechanical Properties.* Physical Review Letters, 2000. **84**(24): p. 5552-5555.

39. Yi, T., L. Li, and C.-J. Kim, *Microscale material testing of single crystalline silicon: process effects on surface morphology and tensile strength.* Sensors and Actuators A: Physical, 2000. **83**(1): p. 172-178.

40. Petersen, K.E., *Silicon as a mechanical material.* Proceedings of the IEEE, 1982. **70**(5): p. 420-457.

41. Hopcroft, M.A., W.D. Nix, and T.W. Kenny, *What is the Young's Modulus of Silicon?* Journal of Microelectromechanical Systems, 2010. **19**(2): p. 229-238.

42. Boyer, N.E., L. Pei, J. Rowley, D. Syme, S. Liddiard, J. Abbott, K. Larson, Z. Liang, B. Iverson, R. Vanfleet, and R. Davis, *Microfabrication with smooth thin carbon nanotube composite sheets.* Materials Research Express, 2017. **4**(3): p. 035032.

43. Hanna, B.H., W.C. Fazio, J.D. Tanner, J.M. Lund, T.S. Wood, R.C. Davis, R.R. Vanfleet, and B.D. Jensen, *Mechanical property measurement of carbon infiltrated carbon nanotube structures for compliant micromechanisms.* Journal of Microelectromechanical Systems, DOI 10.1109/JMEMS.2014.2312847, 2014.

44. Chen, G., B. Dodson, D.M. Hedges, S.C. Steffensen, J.N. Harb, C. Puleo, C. Galligan, J. Ashe, R.R. Vanfleet, and R.C. Davis, *Fabrication of high aspect ratio millimeter-tall free-standing carbon nanotube-based microelectrode arrays.* ACS Biomaterials Science & Engineering, 2018.

45. Stevens, K.A., C.D. Esplin, T.M. Davis, D.J. Butterfield, P.S. Ng, A.E. Bowden, B.D. Jensen, and B.D. Iverson, *Superhydrophobic, carbon-infiltrated carbon nanotubes on Si and 316L stainless steel with tunable geometry.* Applied Physics Letters, 2018. **112**: p. 211602.

46. Brownlee, B.J., M. Bahari, J.N. Harb, J.C. Claussen, and B.D. Iverson, *Electrochemical glucose sensors enhanced by methyl viologen and vertically aligned carbon nanotube channels.* ACS Applied Materials & Interfaces, 2018. **10**: p. 28351–28360.

47. Swanepoel, R., *Determination of surface roughness and optical constants of inhomogeneous amorphous silicon films.* Journal of Physics E: Scientific Instruments, 1984. **17**(10): p. 896.

48. Jahed, H. and A. Tajik, *Standalone Tensile Testing of Thin Film Materials for MEMS/NEMS Applications*, in *Microelectromechanical Systems and Devices*, N. Islam, Editor. 2012, InTech.

49. Ruud, J.A., D. Josell, F. Spaepen, and A.L. Greer, *A new method for tensile testing of thin films.* Journal of Materials Research, 1993. **8**(1): p. 112-117.

50. Johan. Vlassak, J., *New experimental techniques and analysis methods for the study of the mechanical properties of materials in small volumes*. 1994: Stanford University. 312.

51. Vlassak, J.J. and W.D. Nix, *New bulge test technique for the determination of Young's modulus and Poisson's ratio of thin films.* Journal of Materials Research, 1992. **7**(12): p. 3242-3249.

52. Paviot, V.M., J.J. Vlassak, and W.D. Nix, *Measuring the mechanical properties of thin metal films by means of bulge testing of micromachined windows*, in *Materials Research Society Symposium*. 1995, Materials Research Society: Boston, MA. p. 579-584.

53. Robi, K., N. Jakob, K. Matevz, and V. Matjaz, *Current Issues in Sports and Exercise Medicine: The Physiology of Sports Injuries and Repair Processes*. Current Issues in Sports and Exercise Medicine, ed. M. Hamlin. 2012, DOI: 10.5772/56649: IntechOpen.

54. Tissakht, M. and A.M. Ahmed, *Tensile stress-strain characteristics of the human meniscal material.* Journal of Biomechanics, 1995. **28**(4): p. 411-422.

55. Shi, X., X. He, L. Wang, and L. Sun, *Hierarchical-structure induced adjustable deformation of super carbon nanotubes with radial shrinkage up to 66%.* Carbon, 2017. **125**: p. 289-298.

56. Shang, Y., Y. Wang, S. Li, C. Hua, M. Zou, and A. Cao, *High-strength carbon nanotube fibers by twist-induced self-strengthening.* Carbon, 2017. **119**: p. 47-55.

57. Zhang, M., K.R. Atkinson, and R.H. Baughman, *Multifunctional Carbon Nanotube Yarns by Downsizing an Ancient Technology.* Science, 2004. **306**(5700): p. 1358.

58. Miao, M., J. McDonnell, L. Vuckovic, and S.C. Hawkins, *Poisson's ratio and porosity of carbon nanotube dry-spun yarns.* Carbon, 2010. **48**(10): p. 2802-2811.

59. Boyer, N.E., *Microfabrication with Smooth, Thin CNT/Polymer Composite Sheets.* BYU Theses and Dissertations, 2016. **5923**.

60. Liew, K.M., C.H. Wong, and M.J. Tan, *Tensile and compressive properties of carbon nanotube bundles.* Acta Materialia, 2006. **54**(1): p. 225-231.

61. Iijima, S., *Helical microtubules of graphitic carbon.* nature, 1991. **354**(6348): p. 56.

62. Yu, M.-F., O. Lourie, M. J. Dyer, K. Moloni, T. Kelly, and R. Ruoff, *Strength and Breaking Mechanism of Multiwall Carbon Nanotubes Under Tensile Load.* Science, 2000. **287**: p. 637-640.

63. Hutchison, D.N., N.B. Morrill, Q. Aten, B.W. Turner, B.D. Jensen, L.L. Howell, R.R. Vanfleet, and R.C. Davis, *Carbon Nanotubes as a Framework for High-Aspect-Ratio MEMS Fabrication.* Journal of Microelectromechanical Systems, 2010. **19**(1): p. 75-82.

64. Chandrashekar, A., S. Ramachandran, G. Pollack, J.S. Lee, G.S. Lee, and L. Overzet, *Forming carbon nanotube composites by directly coating forests with inorganic materials using low pressure chemical vapor deposition.* Thin Solid Films, 2008. **517**(2): p. 525-530.

65. Akapo, S.O., J.M.D. Dimandja, D.R. Kojiro, J.R. Valentin, and G.C. Carle, *Gas chromatography in space.* Journal of Chromatography A, 1999. **843**(1): p. 147-162.

66. Sternberg, R., C. Szopa, D. Coscia, S. Zubrzycki, F. Raulin, C. Vidal-Madjar, H. Niemann, and G. Israel, *Gas chromatography in space exploration: Capillary and micropacked columns for in situ analysis of Titan's atmosphere.* Journal of Chromatography A, 1999. **846**(1): p. 307-315.

67. Szopa, C., U.J. Meierhenrich, D. Coscia, L. Janin, F. Goesmann, R. Sternberg, J.F. Brun, G. Israel, M. Cabane, R. Roll, F. Raulin, W. Thiemann, C. Vidal-Madjar, and H. Rosenbauer, *Gas chromatography for in situ analysis of a cometary nucleus: IV. Study of*

capillary column robustness for space application. Journal of Chromatography A, 2002. **982**(2): p. 303-312.

68. Contreras, J.A., A. Wang, A.L. Rockwood, H.D. Tolley, and M.L. Lee, *Dynamic thermal gradient gas chromatography.* Journal of Chromatography A, 2013. **1302**: p. 143-151.

69. Contreras, J.A., A.L. Rockwood, H.D. Tolley, and M.L. Lee, *Peak sweeping and gating using thermal gradient gas chromatography.* Journal of Chromatography A, 2013. **1278**: p. 160-165.

70. Sun, J.H., D.F. Cui, X. Chen, L.L. Zhang, H.Y. Cai, and H. Li, *A micro gas chromatography column with a micro thermal conductivity detector for volatile organic compound analysis.* Review of Scientific Instruments, 2013. **84**(2): p. 025001.

71. Kyu Kim, S., H. Chang, and E. T Zellers, *Microfabricated Gas Chromatograph for the Selective Determination of Trichloroethylene Vapor at Sub-Parts-Per-Billion Concentrations in Complex Mixtures.* Analytical Chemistry, 2011. **83**: p. 7198-206.

72. Shih, C.-Y., Y. Chen, and Y.-C. Tai, *Parylene-strengthened thermal isolation technology for microfluidic system-on-chip applications.* Sensors and Actuators A: Physical, 2006. **126**(1): p. 270-276.

73. Rubey, W.A., *An instrumentation assembly for studying operational behavior of thermal gradient programmed gas chromatography.* Review of Scientific Instruments, 1994. **65**(9): p. 2802-2807.

74. Gauthier, B.M., S.D. Bakrania, A.M. Anderson, and M.K. Carroll, *A fast supercritical extraction technique for aerogel fabrication.* Journal of Non-Crystalline Solids, 2004. **350**: p. 238-243.

75. Jensen, D., S. Kanyal, N. Madaan, A. J. Miles, R. Davis, R. Vanfleet, M. A. Vail, A. Dadson, and M. Linford, *Ozone priming of patterned carbon nanotube forests for subsequent atomic layer deposition-like deposition of SiO2 for the preparation of microfabricated thin layer chromatography plates.* Journal of Vacuum Science & Technology B: Microelectronics and Nanometer Structures, 2013. **31**(3): p. 031803-1.

76. Guy, W.W. and W.E. Ellis, *Vacuum Chamber Heat-Transmission Analysis*. 1967, National Aeronautics and Space Administration: Houston, TX. Report No. NASA-TM-X-65036.

77. Mulford, R.B., V.H. Dwivedi, M.R. Jones, and B.D. Iverson, *Control of Net Radiative Heat Transfer With a Variable-Emissivity Accordion Tessellation.* Journal of Heat Transfer, 2019. **141**(3): p. 032702-032702-10.

78. Bergman, T.L., D.P. DeWitt, F. Incropera, and A.S. Lavine, *Fundamentals of Heat and Mass Transfer*. 7 ed. 2011, Hoboken, NJ John Wiley & Sons.

79. Soleimani Dorcheh, A. and M.H. Abbasi, *Silica aerogel; synthesis, properties and characterization.* Journal of Materials Processing Technology, 2008. **199**(1): p. 10-26.

80. Ho, H.-N. and L.A. Jones, *Contribution of thermal cues to material discrimination and localization.* Perception & Psychophysics, 2006. **68**(1): p. 118-128.

81. *CRC Handbook of Chemistry and Physics*. 86 ed. 2005, Boca Raton, FL: CRC Press (an imprint of Taylor and Francis Group).

82. Young, H.D. and F.W. Sears, *University physics*. 1992, Reading, Mass.: Addison-Wesley Pub. Co.

83. Jelle, B.P., A. Gustavsen, and R. Baetens, *The path to the high performance thermal building insulation materials and solutions of tomorrow.* Journal of Building Physics, 2010. **34**(2): p. 99-123.

84. D. Willey, A., J. M. Holt, B. Larsen, J. L. Blackburn, S. Liddiard, J. Abbott, M. Coffin, R. R. Vanfleet, and R. Davis, *Thin films of carbon nanotubes via ultrasonic spraying of suspensions in N-methyl-2-pyrrolidone and N-cyclohexyl-2-pyrrolidone.* Journal of Vacuum Science & Technology B: Microelectronics and Nanometer Structures, 2014. **32**: p. 011218.

85. Fan, J., L. K. Barrett, R. Davis, R. R. Vanfleet, and J. Harb, *The Impact of Encapsulation on Lithium Transport and Cycling Performance for Silicon Electrodes on Aligned Carbon Nanotube Substrates.* Journal of The Electrochemical Society, 2017. **164**: p. A848-A858.